APPLIED RESEARCH

Assessment of the Bundle SNSPD Plus FPGA-Based TDC for High-Performance Time Measurements

FABIO GARZETTI [1], (Member, IEEE), **NICOLA LUSARDI** [1], (Member, IEEE),
ENRICO RONCONI [1], (Member, IEEE), **ANDREA COSTA** [1], (Member, IEEE),
SANTIAGO TARRAGO VELEZ [2], **CHRISTOPHE GALLAND** [3],
AND ANGELO GERACI [1], (Senior Member, IEEE)

[1]Department of Electronics, Information and Bioengineering (DEIB), Politecnico di Milano, 20133 Milano, Italy
[2]Quantum Physics and Information Technology, Danmarks Tekniske Universitet (DTU) Fysik, 2800 Lyngby, Denmark
[3]Laboratory of Quantum and Nano-Optics, EPFL, 1015 Lausanne, Switzerland

Corresponding author: Nicola Lusardi (nicola.lusardi@polimi.it)

ABSTRACT Counting single photons and measuring their arrival time is of crucial importance for imaging and quantum applications that use single photons to outperform classical techniques. The investigation of the coincidence, i.e. correlation, between photons can be used to enhance the resolution of optical imaging techniques or to transmit information using quantum cryptography. Time measurements at the state-of-the-art are performed using Superconducting Nanowire Single Photon Detectors (SNSPDs), the lowest timing jitter single-photon detectors, connected to digital oscilloscopes or digitizers. This method is not well adapted to the ever-increasing and pressing requirement to perform measurements on a high number of channels at the same time. We focus the high-performance measure of the arrival time of photons and their correlation by means of SNSPDs and a 16-channel Time-to-Digital Converter fully implemented in Field Programmable Gate Array (FPGA). In this approach, the photons' coincidence is analyzed in real-time directly in the FPGA, resulting in a Coincidence Time Resolution (CTR) of 22.8 ps r.m.s.. For the practical benefit of the scientific community, an extended and comprehensive panorama also of comparison with the actual available strategies in this field of applications is offered through a huge number of references.

INDEX TERMS Time-to-digital converter (TDC), superconducting nanowire single photon detector (SNSPD), jitter, coincidence time resolution (CTR), field programmable gate array (FPGA).

I. INTRODUCTION

Photon absorption enables for very sensitive light detection by monitoring the transition of a segment of a current-biased superconducting nanowire from superconducting to conventional resistive state [1]. Superconducting Nanowire Single Photon Detectors (SNSPDs) are devices that use this working mode and are used in a variety of quantum information applications [2], [3], quantum computing [4], and quantum optic [5], [6], [7], due to the fact that they are extremely suitable to detect solitary photons [8] with very high probability in a wide spectrum window from UV to infrared [9], [10]. SNSPDs have been used to monitor the emission of single photons from a variety of light sources, including carbon nanotube dopants [11], color centers of silicon carbide [12], and semiconductor quantum dots [13]. Thanks to the absence of a PN-junction, SNSPDs have several advantages over conventional devices that are sensitive to single photons like Single-Photon Avalanche Diode (SPAD), including no afterpulsing (i.e., the triggering of a PN-junction-based detector after the main avalanche effect due to the presence of trap levels that receive extra energy during the first avalanche), extremely low timing jitter, and a low Dark Count Rate (DCR) (i.e., the detection of thermal photons due to the thermal noise in a PN-junction-based detector induced by the generation-recombination processes within

The associate editor coordinating the review of this manuscript and approving it for publication was Remigiusz Wisniewski [ID].

the semiconductor), according to [14]. They are the best detector for applications that require great time precision and excellent weak signal detection. High-resolution light detection and ranging, photon correlations (LIDAR) [15], [16], [17], [18] oxygen singlet detection [19], optical reflectometry in the time domain for telecommunication networks [20], This type of technology was also demonstrated valid in deep-space optical communication by [21], [22]. Furthermore, determining the coincidence (i.e., correlation) between them is required in the calculation of photon arrival time at high-resolution [23]. In particular, the Coincidence Time Resolution (CTR) is one of the most important metrics in this regard [24].

To assign a timestamp to the photons, we can use either a classic Voltage-Mode (VM) [25], [26] or a modern Time-Mode (TM) approach [27], [28]. A Digital Oscilloscope (DO) or a digitizer [29] is used to amplify and digitize the signals from the detectors in a VM method. This permits the timestamp to be recovered using proper Digital Signal Processing (DSP) techniques including oversampling and interpolation, as described in [30]. Additional changes to the resulting waveforms also allow for compensating of non-ideality, such as pile-up. Instead, if a TM technique is used, the signals from the detectors' output are discriminated using a Threshold Comparator (TC) or a Constant Fraction Discriminator (CFD), and then transformed directly into a timestamp using a Time-to-Digital Converter (TDC) [31], [32], [33].

As a result, TM acquisition chains use less hardware than VM acquisition chains and are therefore preferable in multichannel applications. Due to the inability to run DSP algorithms to account for non-ideality, we usually receive less time precision in TM systems than in VM systems. However, by interposing appropriate filters between the detector and the discriminator, we can adjust for these non-idealities and increase timing precision. In this regard, the growing number of channels in modern applications mandates the employment of TM approaches rather than VM approaches, which are now only utilized for preliminary testing.

To implement a TDC, we can use a static Application Specific Integrated Circuit (ASIC) or a programmable logic device, specifically a Field Programmable Gate Array (FPGA) [31]. In this regard, we must keep in mind that an ASIC TDC surpasses an FPGA solution in terms of precision and resolution at the same technological node, but it loses flexibility. In actuality, using an FPGA-based approach allows you to fine-tune the TDC's parameters (resolution, hardware occupancy, number of channels, and so on) to guarantee that the TDC is well-suited to the application. Furthermore, all of the application's processing requirements (e.g., timestamp manipulation, correlation computation, etc.) may be fulfilled directly in the FPGA employing an efficient, high-speed, and flexible parallel computing architecture [32], [33]. This is not achievable with ASIC architectures. In fact, in order to perform correct algorithms, the gathered timestamps must be moved to an appropriate processing unit, such as a Personal Computer (PC), increasing the system

complexity in terms of hardware and/or throughput. In this paper, we show that timing measurements on SNSPD (the most time-resolved detector) may be done with precision referenced to single-shot operating mode less than $26\,psr.m.s.$ up to $1\,MHz$ rate of measure at the current state-of-the-art. Furthermore, we will show how to directly measure the CTR in FPGA while also determining whether two photons detected on two different SNSPDs are in coincidence or not; with this technique, a precision of less than $33.4\,psr.m.s.$ is guaranteed up to a $980\,kHz$ coincidence rate, implying $7\,Mcps$ per detector. As a result, all of the algorithms are parallelized and hosted in the FPGA, with the PC functioning only as a monitor. The organization of the paper is as follows: in Section II, we will provide the current state-of-the-art of time measurement by SNSPD. In Section III, the characteristics of the employed SNSPDs are discussed, and in Section IV, measurements using a VM technique are carried out and used as a reference. Sections V, VI, and VII are where the paper's core and novelty are found, with simulation of temporal jitter (Section VI) and real-time CTR measurement with an FPGA-based TDC (Sections V and VII). Section VIII examines the relationship between measures and possible future development.

II. STATE-OF-THE-ART

The SNSPD is a grid of superconducting nanowires kept at a low temperature, with bias currents (I_{BIAS}) in the μA range provided by a "real" current generator with impedance R_{BIAS}. The low temperature ensures the presence of the so-called superconducting state, in which the material has an infinite conductance and there is no voltage drop across the array. When a photon strikes a nanowire, it warms the area of impact, breaking the superconducting state, according to [1]. As a result, a resistance greater than zero (R_{SNSPD}) emerges for a few ps, generating a pulse of a few mV. The cooling device then restores superconductivity by extracting the heat produced by the detected photon. A graphical depiction of the detecting technique is shown in Figure 1

Despite the low work temperature, some thermal photons can be caught inadvertently by the SNSPD, resulting in a DCR proportional to I_{BIAS} of a few hundreds of cps. Instead, we refer to the likelihood of correctly detecting an optical photon as System Detection Efficiency (SDE); the SDE is also proportional to I_{BIAS} with linear dependency in the so-called "linear region," where the SDE value is between 15% and 85% [10].

An amplification stage (Figure2) is required to amplify the small generated pulse while also shaping it with an exponential waveform of hundreds of mV as amplitude (A), a decay time constant (τ) of a few ns, and a rise time (t_{RISE}) as fast as possible, according to [34]. Using an appropriate instrumentation time-interval-meter (TIM), such as an DO and/or a TDC, it is possible to assign a timestamp to the detected photon, measuring the time instant when the exponential curve rises (Figure 3).
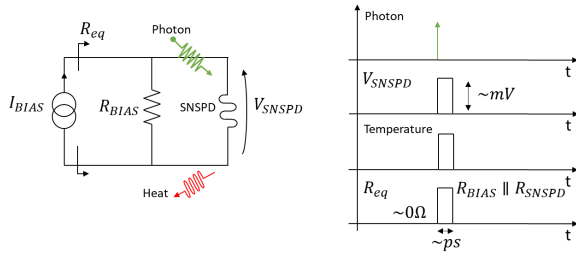
FIGURE 1. An SNSPD's bias (top) and photon detection mechanism (bottom) are depicted graphically.
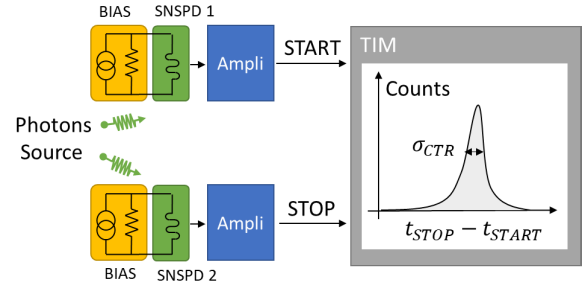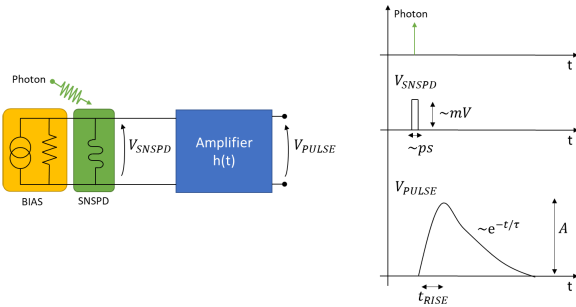

FIGURE 2. The *mV* input pulse (V_{SNSPD}) and the exponential form as output (V_{PULSE}) are reported during the amplification step.
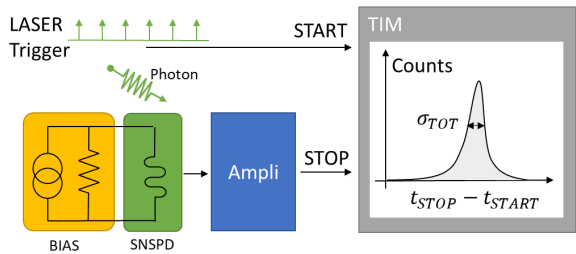

FIGURE 3. Between the SNSPD output and the LASER trigger, a block diagram of a traditional timestamp measurement is shown.

The jitter associated with the exponential curve with regard to the instant of photon detection is attributable, in first approximation, to the inherent jitter that impacts the SNSPD (σ_{SNSPD}) [35] and the electronic jitter introduced by the amplifier noise (σ_{AMPLI}) [36]. However, the investigation in [37] suggests that a third jitter contribution, the jitter of the incident photon (σ_{PHOTON}), be addressed. In fact, from a pure metrological standpoint, it is impossible to determine the instant of creation of the observed photon with infinite precision. When evaluating the SNSPD's characterization experiment, incident photons are sometimes generated by a LASER; thus, σ_{PHOTON} is the jitter in comparison to the ideal trigger. As a result, we may deduce that the measured timestamp is additionally influenced by a fourth component of jitter (σ_{MEAS}) caused by the measurement procedure. The overall jitter (σ_{TOT}), according to Equation (1), is:

$$\sigma_{TOT}^2 = \sigma_{SNSPD}^2 + \sigma_{AMPLI}^2 + \sigma_{MEAS}^2 + \sigma_{PHOTON}^2 \quad (1)$$

FIGURE 4. Block diagram of the CTR.

The measurement of the temporal difference of photons in coincidence over two SNSPDs (Figure 4) is another important application of SNSPDs [37]. A source generates photons at the same moment, which are detected by two distinct SNSPDs in this situation. The spatial position where the photons were generated can be determined by measuring the difference in time of the detected photons. The precision of this measure is the so called CTR and is the standard deviation of the distribution of coincidence measurements (σ_{CTR}). In the same way as σ_{TOT}, the σ_{CTR} depends on the measurement process (σ_{MEAS}) and on the intrinsic and electronic jitters of the two SNSPDs, that is $\sigma_{SNSPD,1}$, $\sigma_{AMPLI,1}$, $\sigma_{SNSPD,2}$, and $\sigma_{AMPLI,2}$ respectively. Precisely, $\sigma_{PHOTONS}$ (photons not photon as in Equation (1)) defines the possible jitter between the coincidence photons that is detected by the SNSPDs due to the nature of physical generation mechanism.

This is summarized in the following equation,

$$\begin{aligned} \sigma_{CRT}^2 = {} & \sigma_{SNSPD,1}^2 + \sigma_{AMPLI,1}^2 \\ & + \sigma_{SNSPD,2}^2 + \sigma_{AMPLI,2}^2 \\ & + \sigma_{MEAS}^2 + \sigma_{PHOTONS}^2 \end{aligned} \quad (2)$$
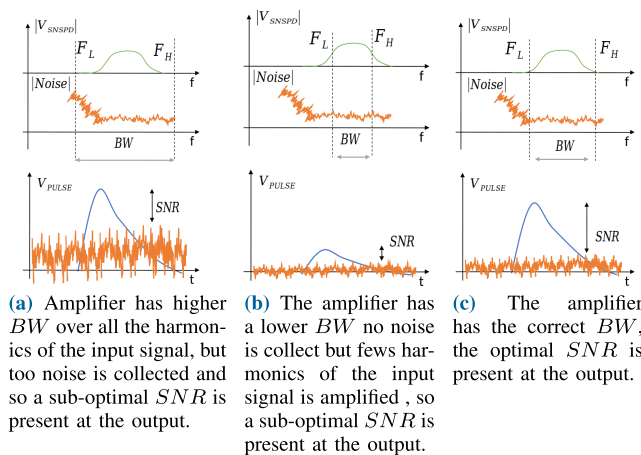
The symmetry between the two SNSPDs makes feasible to set $\sigma_{SNSPD,1} = \sigma_{SNSPD,2} = \sigma_{SNSPD}$ and $\sigma_{AMPLI,1} = \sigma_{AMPLI,2} = \sigma_{AMPLI}$, reducing Equation (2) to

$$\begin{aligned} \sigma_{CRT}^2 = {} & 2 \cdot (\sigma_{SNSPD}^2 + \sigma_{AMPLI}^2) \\ & + \sigma_{MEAS}^2 + \sigma_{PHOTONS}^2 \end{aligned} \quad (3)$$

A. INTRINSIC JITTER

The I_{BIAS} [35], [36], the cooling temperature (T_K) [38], the active area, a.k.a. geometry of the grid array, (A) [36], [39], and the wavelength (λ) of the detected photon all influence the σ_{SNSPD}. From an intuitive standpoint, the shorter the λ or the lower the T_K, the faster the state transition from superconducting to non-superconducting, lowering the σ_{SNSPD}, i.e., $\sigma_{SNSPD} \propto \lambda$ and $\sigma_{SNSPD} \propto T_K$. Similarly, if I_{BIAS} is increased or the A is decreased, the voltage pulse has a faster response, which reduces the inherent jitter, i.e., $\sigma_{SNSPD} \propto 1/I_{BIAS}$, and $\sigma_{SNSPD} \propto 1/A$.

Obviously, there are just a few alternatives for tuning these four factors. First and foremost, an SNSPD's job is to detect photons with a λ that cannot normally be modified and is

(a) Amplifier has higher BW over all the harmonics of the input signal, but too noise is collected and so a sub-optimal SNR is present at the output.

(b) The amplifier has a lower BW no noise is collect but fews harmonics of the input signal is amplified , so a sub-optimal SNR is present at the output.

(c) The amplifier has the correct BW, the optimal SNR is present at the output.

FIGURE 5. The spectrum of the pulse signal produced by photon detection of a generic SNSPD (green), amplifier BW (gray), noise (orange), and time-domain amplified signal (blue) in three different conditions.

determined by the nature of the processes being studied. Furthermore, for a certain application, a minimum A is desired, which determines the device's geometry (i.e., thickness, fill-factor, width, and length). A preset upper limit to the I_{BIAS} is also set to keep the DCR low. Furthermore, there is a technological restriction to the minimum T_K.

In practice, SNSPDs exhibit intrinsic jitter in the range of 6 ps to 20 ps as FWHM, taking these factors into account [40].

B. ELECTRONIC JITTER
As can be seen, σ_{AMPLI} is highly dependent on the amplifier's Noise Figure (NF), Gain (G), and Band Width (BW). In fact, σ_{AMPLI} results in a random dispersion of the exponential's rising edge in relation to the voltage pulse in input [41]. As a result, the identical input voltage pulse creates very distinct exponential waveforms, increasing the detection event's uncertainty. To reduce this dispersion, we must ensure that the output exponential shape (t_{RISE}) has a steep rising edge, so $\sigma_{AMPLI} \propto 1/t_{RISE}$, with the highest possible Signal-to-Noise Ration (SNR) [35], which is equivalent to minimizing NF, $\sigma_{AMPLI} \propto NF$, and maximizing G, $\sigma_{AMPLI} \propto 1/G$.

In general, we need to ensure tens of dB as G. in order to achieve the goal output amplitude of hundreds of mV.

To prevent collecting noise, we must select an amplifier with a BW that is as close as feasible to the spectrum of the input voltage pulse contained between the boundary down (F_L), imputable to the the 1/f noise corner frequency (F_C), and up frequencies, (F_H) (Figure 5). We will get a t_{RISE} that is inversely proportional to F_H, i.e., $t_{RISE} \sim 1/F_H$ [42]. Using ultra-fast RF amplifiers with F_H of several GHz, t_{RISE} of hundreds of ps is ensured. The presence of the 1/f noise with F_C of hundreds of kHz impose the F_L in the same order of magnitude. In addition, even in the presence of pile-up, a minimum recovery time into the superconducting state is necessary for linearity in the count rate. In [34] an upper limit of tens of ns for the exponential decay time constant

(τ) is set. Given that τ is inversely proportional to F_L in the first approximation, i.e. $\tau \sim 1/F_L$. Considering this two contribution, τ has upper limit of tens of ns.

Figure 6 shows a graphical equivalence between the amplifier's output exponential and its Bode diagram for completeness. Table 1 recaps all of the amplifier's parameters in relation to their restrictions.

As a result, in real-world applications, we see electronic jitter ranging from 14 to 45 ps as FWHM [37].
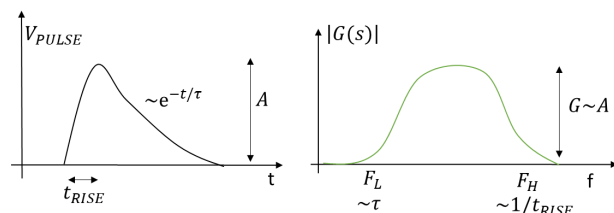
FIGURE 6. The amplifier's output exponential and its Bode diagram are compared.

TABLE 1. A list of the amplifier's parameters, together with their limitations and numerical values.

Parameters	Constraint	Value
G	The ratio of the SNSPD's amplitude to the request exponential form.	$10 \div 100\,dB$
NF	Reduce basis of noise to keep high the SNR	$< 10\,dB$
F_H (t_{RISE})	Reduce the collected noise to keep high the SNR	$< 10\,GHz$ ($> 100\,ps$)
F_L (τ)	Guarantee a proper recovery time and keep high the SNR (1/f noise)	$< 100\,MHz$ ($> 10\,ns$)

C. MEASUREMENT JITTER
The contribution of σ_{MEAS} relies on the device used for timestamping, i.e. the more precise the instrument, the lower the contribution of σ_{TOT} and σ_{CTR}. In this instance, the rule of thumb is to use a high-precision instrument (a.k.a. σ_{MEAS}), which is sigma $\sigma_{MEAS}^2 \ll \sigma_{SNSPD}^2 + \sigma_{AMPLI}^2$ in this example. This restricts the precision requested to some ps in real-world applications.

Oscilloscopes and time-interval-meters are the two types of equipment we can utilize, as expected. Due to the tremendous success of digital electronics and digital signal processing, we propose to use the DO as an oscilloscope and the TDC as a time-interval-meter.

1) DIGITAL OSCILLOSCOPE
In the case of DO, the amplifier's exponential output form is sampled as a classical analog signal with a sampling frequency F_S according to Shannon theorem (i.e., $F_S \geq 2 \cdot F_H$). This involves working with a sampling rate of tens of $Gsps$, which translates to a timestamp resolution of only hundreds of ps (LSB). In fact, the accuracy provided by a DO (σ_{DO})

is proportional, in the ideal case, to the LSB (i.e., $\sigma_{DO} = LSB/\sqrt{12}$) and in the absence of interpolation techniques $LSB = 1/F_S$. To lower σ_{DO} to a few ps, a digital oversampling of the collected waveform and a subsequent interpolation technique (e.g., sinc) are required.

The DO method allows you to examine the exponential structure in greater detail, but it has several limitations. To begin, at least one byte every sample is required to make the interpolation technique successful; this translates to tens of $GByte$ per second of data that must be stored during the acquisition, which is thus limited in duration. Furthermore, the DO technology has a strict limit on the number of parallel channels that may be used, making this approach practical solely for detector characterization. In this regard, the TDC technique is required for the majority of applications.

2) TIME-TO-DIGITAL CONVERTER APPROACH

The exponential output form is directly translated into a timestamp at 32 or 64 bits with a few ps of LSB using the TDC method. In this method, no post-processing for interpolation is required, and data storage is reduced, allowing the system to run in real-time. Obviously, the shape information is completely gone.

The TDC assigns a timestamp to the input signal referring to on an internal clock (time-tagger) [43] or an external event event (start-stop), as described in [44]. The start-stop approach and are commonly used in Time Correlated Single Photon Counting (TCSPC) applications; on the other hand, the time-tagging solutions can work in continuous mode. The concept of time measurement is defined as the time elapsed between an absolute time reference, taken as "zero" on the time axis, and the occurrence of a certain event of interest. In this case, our measurement is a "Timestamp"; however, we are usually more interested to carry out a time measurement as the relative "Time Distance" between two events, the first one being the "START" signal, and the second being the "STOP" signal. Anyhow, a "Timestamp" is nothing but a particular case of time distance between a chosen absolute time reference, and the event under study. On the other hand, the time distance between two events is the time difference between their timestamps, each one calculated referencing to a common absolute "zero" time origin. Figure 7 shows the concept just explained.
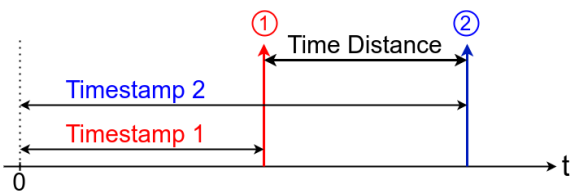

FIGURE 7. Graphical representation of the concepts of "Timestamp" and "Time Distance".

The primary difference between TDCs, regardless of operating mode, is in the circuit architecture and technology employed for time-to-digital conversion. In reality, we have

the option of using a mixed-signal or all-digital technique. The Time-to-Amplitude Converter (TAC) [45] is the most popular and widely used mixed-signal TDC, in which the time interval is transformed into a voltage level and monitored by an Analog-to-Digital Converter (ADC). Instead, the most widely used fully-digital TDCs are based on the Delay-Line (DL), in which the time interval is quantized using the propagation delay of the logic gate that composes the DL and specifies the LSB, regardless of the individual circuit [46].

Mixed-signal and fully-digital TDCs can both be implemented as ASIC, while fully-digital TDCs can also be implemented in FPGA devices [47].

The designer of an ASIC solution can fine-tune all of the circuit's settings with considerable freedom in order to obtain the best performance. Modern FPGA technologies now enable for equivalent performance in a considerably shorter time-to-market while also having a far reduced overhead than an ASIC approach. The extreme high flexibility of FPGA-based systems makes them increasingly more recommended at equal accuracy levels [48].

3) COMPARISON

Table (2), which refers to Paragraphs II-C1 and II-C2, concentrates on the advantages and disadvantages of DO and TDC techniques. Table (3) shows the precision and maximum number of parallel channels based on the SNSPD literature [49].

TABLE 2. In SNSPD timestamp acquisition, the advantages and disadvantages of the DO and TDC approaches are compared.

Feature	DO	TDC
Precision	great	average
Acquired data	great	small
Parallelism	low	great
Real-time	no	yes
Cost	great	small

TABLE 3. On SNSPD-related literature, precision (σ_{MEAS}) and maximum number of parallel acquisitions (N_{CH}) were done.

| Methodology	$\sigma_{MEAS}\ [ps\ r.m.s]$	N_{CH}	Reference
DO	18	4	[50]
DO	37	4	[51]
TDC (start-stop)	18.4	2	[52]
TDC (start-stop)	18	2	[53]
TDC (start-stop)	17.8	2	[54]
DO	14.8	2	[55]
TDC (start-stop)	17.3	2	[49]
TDC (time-tagging)	58	8	[56]
TDC (time-tagging)	64	170	[57]
TDC (time-tagging)	26	16	This paper

III. SNSPD OVERVIEW

We characterized a two channels detection system provided by Single Quantum B.V. [58] using a LeCroy WaveRunner HRZ640i ([59]) as the DO (Figure8), which is made up of two

FIGURE 8. SNSPD detector bundle from Single Quantum B.V. The two SNSPDs are in the cryostater, which is the red box with the gray tower, the RF amplifiers are in the black box, and the PC is used to set the bias and monitor the DCR and SDE.

channels, each of which is made up of an SNSPD followed by an amplification stage made up of a cascade of two RF Low Noise Amplifiers (LNAs), a ZTL-1000 [60], and an LNA-1000 [61]. It is possible to adjust the I_{BIAS} for each SNSPD in order to properly configure the DCR and SDE.

The detector is a shaped NbTiN nanowire with a width of $100\,nm$ and a fill factor of 50. (Figure 9) [62]. The nanowire structure has a diameter of $16\,\mu m$ and is optically coupled to a mono-modal optical fiber with a diameter of $12\,\mu m$. (Figure 9). The superconductor is placed on top of a resonant cavity made of a $135\,nm$ silicon-oxide layer and gold to increase the likelihood of absorbing photons at about $800\,nm$. Because photon down-conversion sources emit in this wavelength range, this wavelength range is highly valuable for quantum research. The detector is kept at a T_K of $2.5\,K$ using a Gifford-McMahon closed-cycle cryo-cooler.
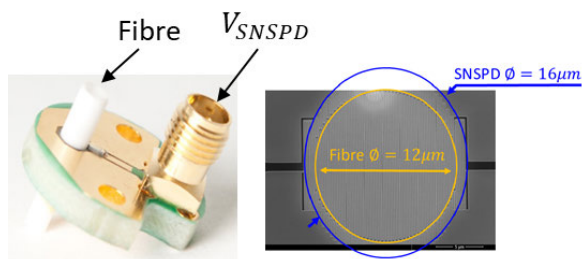
FIGURE 9. Picture of SNSPD with optical coupling from SNSPD (diameter $16\,\mu m$) to the optical fiber (diameter $12\,\mu m$).

The SNSPD, with its I_{BIAS} current generator, is at the input of the amplification stage. When photon detection occurs, the SNSPD's load impedance (i.e., $R_{BIAS}\|R_{SNSPD} \sim k\Omega$) is

greater than the amplifier's input impedance ($Z_{IN} \sim 50\,\Omega$); as a result, I_{BIAS} is deviated from the SNSPD to the amplifier, which generates the voltage pulse $Z_{IN} \cdot I_{BIAS}$.

About the RF amplifiers; the ZTL-1000 features G_{ZTL}^{dB} of $17\,dB$, NF_{ZTL}^{dB} of $6\,dB$, Z_{IN} of $50\,\Omega$, an output impedance (Z_{OUT}) of $50\,\Omega$, F_L of $0.1\,MHz$, and F_H of $1\,GHz$. Instead, the LNA-1000 has G_{LNA}^{dB} of $33\,dB$, NF_{LNA}^{dB} of $2\,dB$, Z_{IN} and Z_{OUT} of $50\,\Omega$, F_L of $10\,MHz$, and F_H of $1\,GHz$. As a result, overall G of $50\,dB$ (i.e., $G_{TOT}^{dB} = G_{ZTL}^{dB} + G_{LNA}^{dB}$) and NF of $5\,dB$ (i.e., $NF_{TOT} = NF_{ZTL} + NF_{LNA}/G_{ZTL}$) are obtained preserving a Z_{IN} and Z_{OUT} of $50\,\Omega$. The BW is limited between $10\,MHz$ and $1\,GHz$ as F_L and F_H, respectively; this is owing, to a first approximation, to the limiting element, the LNA-1000.

Finally, we have created a Simulink model of the SNSPD (Paragraph III-B).

A. SNSPD DESCRIPTION AND CHARACTERIZATION

The calibration curve, SDE vs I_{BIAS}, is measured (using photons with λ of $750\,ns$) to determine the SNSPD's working point.

With a I_{BIAS} of $17\,\mu A$, the SNSPD achieves the saturation with a SDE of 80.7%; so, a "linear region" operating point at I_{BIAS} of $14\,\mu A$ with a SDE of 70% is choose. This SED consider the SPSPD's deception efficiency and all the optical losses.

A Ti:Sapphire LASER with a repetition rate (F_{LASER}) of $76\,MHz$, a pulse width of $6\,ps$, and a λ of $750\,nm$ was then used to illuminate the SNSPD. As a result, the waveform at the detection system's output is sampled (Figure10). An exponential shape with a τ of $14\,ns$ (i.e., $\tau \sim 1/F_L = 1/10\,MHz = 10\,ns$), rising time t_{RISE} of $2\,ns$ (i.e., $\tau \sim 1/F_H = 1/1\,GHz = 1\,ns$), and amplitude ($A$) of $\sim 500\,mV$ (i.e., $A \sim (50\Omega \cdot I_{BIAS})\,G_{TOT} = (50\Omega \cdot 14\mu A)\,10^{50/20} = 221\,mV$) is measured, as predicted by the theory.
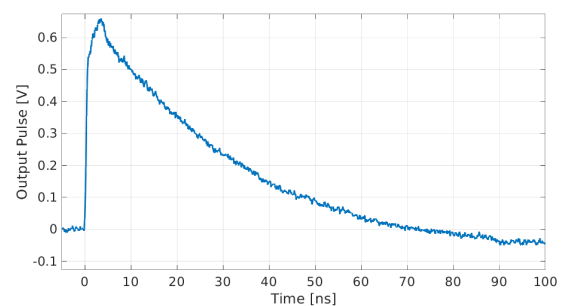
**FIGURE 10.** Image of the signal at the SPSPD's amplification system's output.

B. SNSPD SIMULINK SIMULATION

The SNSPD detection system is recreated in the Simulink environment using the information obtained in Paragraph III-A. To begin, the LASER is simulated using a delta-comb generator with a period $T_{LASER} = 1/F_{LASER}$ of $1/76\,MHz \cong 13.128\,ns$ and active time (T_{ON}) of $6\,ps$. The SNSPD's detection efficiency is replicated using a random generator that

generates a number n between 0 and 100 and suppresses the delta-comb if n is greater than the SDE ($n > SDE$). The SNSPD is modeled using a first-order system with a thermal τ of $100\,ps$, which reflects the time it takes to regain the superconducting state.

The S-parameter model given by Minicircuit (ZTL-100) and RF BAY Inc is used to simulate the two amplifiers (LNA-100). In this method, the LASER is represented by a digital trigger, and the SNSPD is represented by an exponential form.

Figure 11 depicts the simulation model's block architecture, while Figure 12 depicts a comparison of the emulated exponential output with respect to the genuine one.
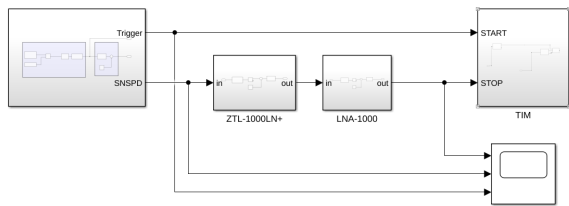
FIGURE 11. This Simulink simulation model shows photon detection emulation, two amplifiers, the TIM for timestamp measurement, and the scope for acquiring "analog" waveforms.
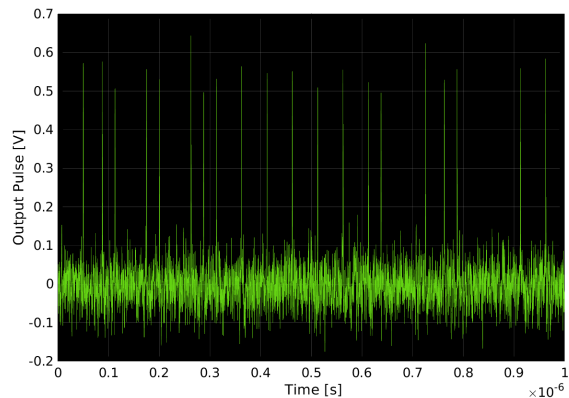
(a) Emulated exponential output observe by the scope on the Simulink environment (Figure 11).
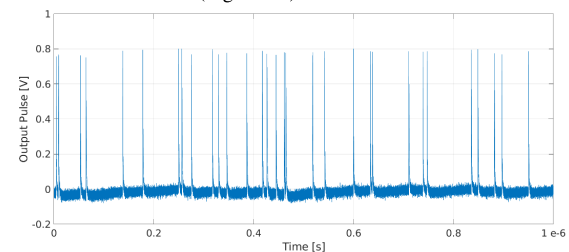
(b) Real exponential output.

FIGURE 12. In this comparison, the simulated exponential output is compared to the real one.

IV. SNSPD TIMESTAMPING WITH OSCILLOSCOPE
A traditional timestamping with a LeCroy WaveRunner 640i as DO operating at 40 GSs and 8-bit, as a first step, before

using the fully-digital solution described in Section V is done. The SNSPD versus LASER characterization is shown in Paragraph (IV-A), and the CTR between two SNSPDs induced by the same LASER is evaluated in Paragraph V.

A. SNSPD VS LASER
The jitter between the SNSPD and the LASER (Figure 3, where TIM we used a LeCroy WaveRunner 640i scope) yields a Gaussian shape with a standard deviation of $19.84\,ps\,r.m.s.$ (i.e., FWHM of $44.27\,ps$) that represents σ_{TOT} stated in Equation (1). To do this, the skew between the SNSPD's analog waveform and the LASER acquired with the DO was measured, and a sinc interpolation was used to provide the maximum possible precision. After that, a statistically significant amount of measurements was used to create a histogram. In this method, we were able to replicate the measurement result reported in Table 4 and in [56].

Furthermore, as illustrated in Figure 13, the pile-up of exponential pulses has caused a baseline fluctuation. In reality, there is superposition and consequently distortion of the $n - th$ SNSPD's exponential curve starts before the tail of the $(n-1)-th$ curve terminates, which is around $5\tau \cong 5 \cdot 14\,ns = 70\,ns$ long. In this case, as shown in Figure 14, generating a timestamp when the SNSPD waveform crosses a specified threshold causes a walk-error. Because the SNSPD randomly triggers on the LASER pulse, the baseline fluctuation is also a random variable with a standard deviation of σ_{BASE}. As a result, the walk-error is random and is defined by the standard deviation σ_{WALK}, which has an impact on the slope (Sl) during the rising edge of the exponential shape of the SNSPD (i.e., $Sl = A/t_{RISE}$) and, obviously,on σ_{BASE},as shown by the relationship

$$\sigma_{WALK} = \frac{\sigma_{BASE}}{Sl} \quad (4)$$

In this sense, the oscilloscope's σ_{MEAS} is made up of two parts: σ_{WALK}, which is due to the baseline and is transformed to time by the discrimination algorithm, and σ_{DO}, which is the quantization error of the DO; i.e.,

$$\sigma_{MEAS}^2 = \sigma_{WALK}^2 + \sigma_{DO}^2 \quad (5)$$

Inserting Equations (4) and (5) in Equation (1), we get

$$\sigma_{TOT}^2 = \sigma_{SNSPD}^2 + \sigma_{AMPLI}^2 \\ + (\frac{\sigma_{BASE}}{Sl})^2 + \sigma_{DO}^2 + \sigma_{PHOTON}^2 \quad (6)$$

In this method, the baseline fluctuation is suppressed using a digital baseline restoration algorithm that implements a correct discrimination to detect the timestamp compensating the σ_{BASE} (i.e., $\sigma_{WALK} \longrightarrow 0\,ps\,r.m.s.$) to achieve the highest level of precision possible. Furthermore, because to a higher probability of pile-up, the size of the baseline is proportional to the count-rate on the SNSPD (R_{SNSPD}), as you might expect. To confirm this, we measured σ_{BASE} and Sl as function of R_{SNSPD} using the DO in a range of 18 to $200\,kHz$, observing an increase in σ_{BASE}; the results are shown in Table 5.

TABLE 4. In [56] Equation (5) is used to reproduce the measurement results exposed by Single Quantum.

Contribution	Value [$ps\ r.m.s.$]
σ_{TOT}	19.84
σ_{SNSPD}	8
σ_{PHOTON}	6
σ_{AMPLI}	14
σ_{WALK}	$\longrightarrow 0$
σ_{DO}	2
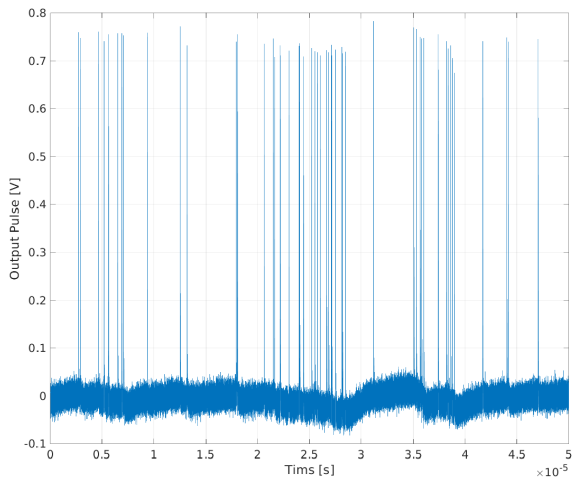
FIGURE 13. The pile-up effect of the SNSPD's exponential output causes baseline fluctuation.

TABLE 5. The σ_{BASE} and Sl measurements as function of the R_{SNSPD}, and σ_{WALK} computation as represented in Equation (4).

R_{SNSPD} [kHz]	σ_{BASE} [$mV\ r.m.s.$]	Sl [V/ns]	σ_{WALK} [$ps\ r.m.s.$]
8.9	2.9	0.76	3.8
18	3.3	0.76	4.3
27	3.2	0.76	4.2
35	3.1	0.76	4.1
55	3.2	0.76	4.2
73.2	3.6	0.76	4.7
102	3.6	0.76	4.7
135	4.2	0.76	5.6
180	4.3	0.76	5.7
200	6.8	0.76	8.9

Due to some non-ideality in the estimation of σ_{SNSPD}, σ_{AMPLI}, σ_{DO}, and the suppression of σ_{WALK}, Table 4 reveals a non-perfect agreement between σ_{TOT} (19.84 $ps\ r.m.s.$) and Equation (5) (i.e., $\sqrt{8^2 + 14^2 + 0 + 2^2 + 6^2} = 17.3 ps\ r.m.s.$). The discrepancy between the predicted value 17.3 $ps\ r.m.s.$ and the actual value 19.84 $ps\ r.m.s.$ yields a quadratic error of $\sqrt{19.84^2 - 17.3^2} = 7.46 ps\ r.m.s.$

B. SNSPD VS SNSPD

We next measured the CTR between two SNSPDs triggered by the same LASER pulse using the LeCroy WaveRunner 640i as DO (Figure 4) tuning on the baseline restore method.
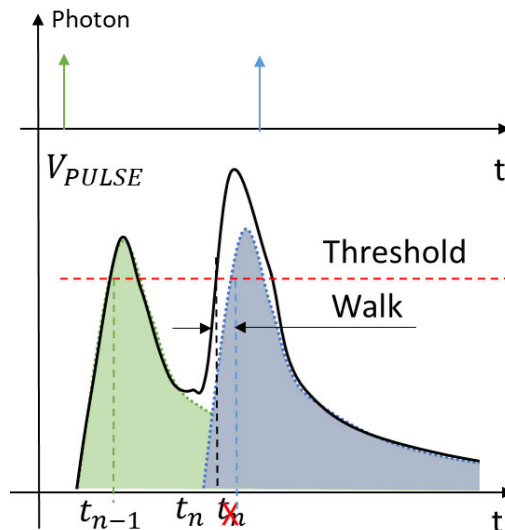
FIGURE 14. The walk-error induced by the pile-up phenomenon is represented here.

Unfortunately, because of the random nature of SNSPDs, real-time activation is difficult. In fact, in order to consider only the SNSPD numbers 1 and 2 in coincidence with the LASER, we must obtain all timestamps and execute post-processing elaboration as shown in Figure 15. The result of the CTR count-rate (R_{CTR}) in the range of 1.2 cps to 720 cps is reported in Table 6. Count-rates in the range of 6.8 $kcps$ and 200 $kcps$ are sought over the two SNSPDs, number 1 and 2 ($R_{SNSPD,1}$ and $R_{SNSPD,2}$ respectively) to guarantee this R_{CTR}.

To compute the CTR in practice, we must apply the statistic to a large number of skews computed between two detected coincidence events over the SNSPDs and extract the standard deviation (σ). To accomplish so, an acquisition time (T_{ACQ}) of a few minutes was required in order to collect at least $\sim 10^4$ of coincidence events (N_{CRT}) (i.e., $N_{CRT} = T_{ACQ} \cdot R_{CRT}$). When we consider the F_S of 40 GHz and the size of each single sample (1 $Byte$), we can calculate that for SNSPD #1 and #2, we need to acquire a total of $N_{SNSPD,1} = F_S \cdot T_{ACQ}$ and $N_{SNSPD,2} = F_S \cdot T_{ACQ}$ samples, which corresponding to 4.68 $TByte$ for each minute of acquisition (i.e., ($N_{SNSPD,1} + N_{SNSPD,2}$) $\cdot$ (1 $Byte$) $\cdot$ (60 $sec/minute$)). As a result, the proposed approach is incompatible with real-time applications. TDC timestamping was introduced to enable real-time measurement.

To change $R_{SNSPD,1}$ and $R_{SNSPD,2}$ while maintaining the I_{BIAS} of the SNSPDs constant, an appropriate optical programmable attenuator with a value of A^{dB} is placed between the LASER and the SNSPDs, reducing the quantity of photons and, as a result, the count-rates.

We may state that, using Equations (3), (4), (5), and the same method used in Paragraph IV-A,

$$\sigma_{CTR}^2 = 2 \cdot (\sigma_{SNSPD}^2 + \sigma_{AMPLI}^2) + (\frac{\sigma_{BASE}}{Sl})^2 + \sigma_{DO}^2 + \sigma_{PHOTONS}^2 \qquad (7)$$
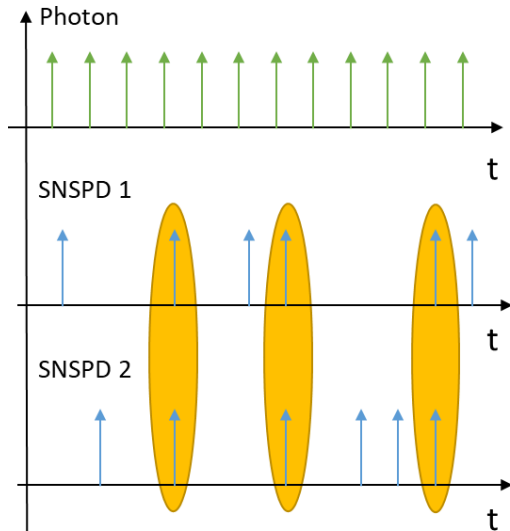
FIGURE 15. The CTR measurement is graphically depicted.

TABLE 6. Measured σ_{CTR} corresponding to different $R_{SNSPD,1}$, $R_{SNSPD,2}$, and R_{CTR} performed in post-processing with the DO.

$R_{SNSPD,1}$ [kHz]	$R_{SNSPD,2}$ [kHz]	R_{CTR} [Hz]	σ_{CTR} [ps r.m.s.]
6.8	8.9	1.2	17.6
15	18	5.4	16.2
23	27	12.4	14.5
31	35	21.7	14.0
48	55	52.8	14.5
63.2	73.2	92.5	13.6
90.6	102	184.8	16.2
133	135	359.1	16.0
160	180	576	14.9
180	200	720	17.0

where $\sigma_{PHOTONS}$ is the jitter between the two correlated emitted photons (a.k.a., photons in coincidence) that will be detected by the SNPSDs for the CTR estimation, as opposed to σ_{PHOTON}, which is the jitter between the LASER and its trigger (i.e., $6\,ps\,r.m.s.$). We can examine $\sigma_{PHOTOS} \rightarrow 0$ in our experimental setup, where the correlated photons are created via a beam splitter. Equation (7) becomes, in this case.

$$\sigma_{CTR}^2 = 2 \cdot (\sigma_{SNSPD}^2 + \sigma_{AMPLI}^2) + (\frac{\sigma_{BASE}}{Sl})^2 + \sigma_{DO}^2 \qquad (8)$$

Moreover, if the baseline fluctuation is made negligible,

$$\sigma_{CTR}^2 = 2 \cdot (\sigma_{SNSPD}^2 + \sigma_{AMPLI}^2) + \sigma_{DO}^2 \qquad (9)$$

We would like to point out that the measured σ_{CTR} values (Table 6), in the range of $14.0\,ps\,r.m.s$ to $17.6\,ps\,r.m.s$, and Equation (9) (i.e., $\sqrt{2(8^2 + 14^2) + 2^2} = 22.8\,ps\,r.m.s.$) have a quadratic error ranges from $14.5\,ps\,r.m.s$ (i.e., $\sqrt{22.8^2 - 17.6^2} = 14.5\,ps\,r.m.s$) to $17.6\,ps\,r.m.s$ (i.e., $\sqrt{22.8^2 - 14.0^2} = 17.6\,ps\,r.m.s$) due to the estimation of σ_{SNSPD}, σ_{AMPLI}, σ_{DO}.
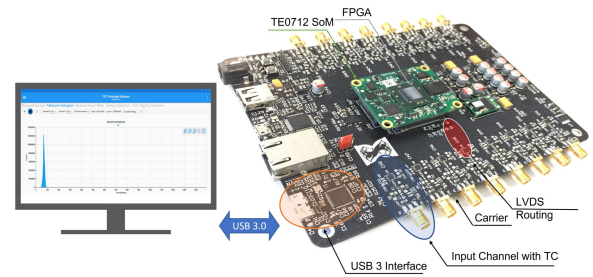

FIGURE 16. Setup overview.

V. SNSPD TIMESTAMPING WITH TDC BUT NO BASELINE COMPENSATION

In this Section, we describe the real-time characterizations of LASER vs SNSPD and SNSPD vs SNSPD performed using a TDC introduced in [33] and applied in numerous scientific investigations [63], [64]. We used the same configurations stated in Section IV, replacing the DO with the TDC in these tests. There is no mechanism in place to filter out baseline fluctuation.

A. INSTRUMENT USED

Figure 16 shows the used configuration, which comprises of a multi-channel Tapped Delay-Line based TDC (TDL-TDC) that has been integrated into an FPGA device [31], [46]. The FPGA is a Xilinx 28-nm 7-Series Artix-7 200T [65], which is mounted on a Trenz Electronics [66] TE0712 System-on-Module (SoM) and connected to a custom carrier board through a large number of connectors. The configuration allows for better software and hardware re-configurability, allowing the user to easily change the FPGA device by simply replacing the TE0712 with SoMs from the same TE07xx family. In multi-channel mode, the TDC can run up to 16 parallel channels at high performance. As shown in Figure 16, the input receives an analog signal ranging from 0 to 3.3 V, which is converted into an LVDS digital pulse by a programmable TC. Differential traces calibrated at $100\,\Omega$ distribute signals to the connectors and to the device where the TDC is located. The power stage and communication resources are housed on the carrier board.

Table 7 highlights the main characteristics of the instrument employed. In connection to the σ_{TDC} mentioned in Sections above, we must understand that it is a combination of the two channel precision (i.e., $\sigma_{CH} = 12\,ps\,r.m.s.$), one for the START timestamps and one for the STOP timestamps used to define the time interval under measurement. In this sense, $\sigma_{TDC}^2 = \sigma_{CH}^2 + \sigma_{CH}^2 = 2\sigma_{CH}^2 = (17\,ps\,r.m.s.)^2$.

The suggested instrument is totally based on FPGA; the TDC and processing are both located in this seance's programmable logic. User-defined real-time parallel methods can be developed, or the collected timestamps can be forwarded to a PC for post-processing manipulation, as with the DO in Section IV. In this sense, a coincidence engine for the CTR has been implemented. Furthermore, a hardware

TABLE 7. Main characteristics of the used TDC.

Feature	Value
Channels	16
Maximum Rate	$20\,MHz$
Resolution (LSB)	$2\,ps$
Precision (σ_{CH})	$12\,ps\,r.m.s.$
Integral Non-Linearity (INL)	$< 4.2\,ps$
Temperature drift	$286\,fs/°C$

histogrammer has been developed to retrieve the statistics of the SNSPD vs LASER (σ_{TOT}) and SNSPD vs SNSPD (σ_{CTR}) directly.

B. SNSPD VS LASER

The identical measurement setup described in Paragraph IV-A and Figure 3, replacing the DO with the TDC presented in Paragraph V-A, is used. The TDC calculates the statistics, such as the histogram, in real time by measuring the time interval between LASER and SNSPD. In this way, we set as references a voltage level that is exactly half of the amplitude of the LASER and SNSPD signals, respectively, to properly activate the timestamp acquisition with regard to the rising-edge of LASER and SNSPD.

Different acquisitions at different R_{SNSPD} values are reported in Table 8. Obviously, there is no compensatory mechanism for baseline fluctuation. As a result, measurements with lesser precision than those obtained with DO are produced.

TABLE 8. Measured σ_{TOT} at different R_{SNSPD} values between LASER and SNSPD using the TDC.

R_{SNSPD} [kHz]	σ_{TOT} [ps r.m.s.]
5	33.8
36	34.6
450	34.8
1000	33.4

By substituting σ_{DO} with σ_{TDC} in Equation (5), we can easily adapt it to the case of the TDC; i.e.,

$$\sigma_{TOT}^2 = \sigma_{SNSPD}^2 + \sigma_{AMPLI}^2 + (\frac{\sigma_{BASE}}{Sl})^2 + \sigma_{TDC}^2 + \sigma_{PHOTON}^2 \quad (10)$$

Considering the presence of walk-error distributed between $3.9\,ps\,r.m.s.$ and $8.9\,ps\,r.m.s.$, as Table 5 highlights, we can theoretically estimate σ_{TOT} that is in the range between $29.5\,ps\,r.m.s.$ (i.e., $\sqrt{8^2 + 14^2 + 3.9^2 + 17^2 + 6^2} = 29.5\,ps\,r.m.s.$) and $29.5\,ps\,r.m.s.$ (i.e., $\sqrt{8^2 + 14^2 + 8.9^2 + 17^2 + 6^2} = 30.5\,ps\,r.m.s.$. The difference between expected and measured values corresponds to a quadratic error distributed in the range between $16.8\,ps\,r.m.s.$ (i.e., $\sqrt{34.8^2 - 30.5^2} = 16.8\,ps\,r.m.s.$) and $15.7\,ps\,r.m.s.$ (i.e., $\sqrt{33.4^2 - 29.5^2} = 15.7\,ps\,r.m.s.$).

C. SNSPD VS SNSPD

We employed the identical setup of measurement utilizing the TDC instead of the DO and computing the CTR in real-time rather than post-processing mode, as shown in Paragraph IV-B and Figure 4. In this method, we were able to compile statistics and determine the time gap between SNSPD and SNSPD using the TDC. As a result, we set as references a voltage level that is exactly half the amplitude of the SNSPD signal in order to properly initiate the timestamp acquisition with respect to SNSPD rising-edges.

For SNSPD #1 ($R_{SNSPD,1}$) and #2 ($R_{SNSPD,2}$), several acquisitions were carried out for different count-rates and summed up in Table 9. In this situation as well, no baseline compensation method is used, resulting in a decrease in CTR precision when the rate is increased.

Replacing σ_{TDC} with σ_{DO}, Equation (8) becomes

$$\sigma_{CRT}^2 = 2 \cdot (\sigma_{SNSPD}^2 + \sigma_{AMPLI}^2) + (\frac{\sigma_{BASE}}{Sl})^2 + \sigma_{DO}^2 \quad (11)$$

So, we can estimate σ_{CTR} considering a walk-error between $3.8\,ps\,r.m.s.$ and $8.9\,ps\,r.m.s.$ obtaining a theoretical value between $28.5\,ps\,r.m.s.$ and $29.7\,ps\,r.m.s.$, which means quadratic error with respect to the experimental value between $17\,ps\,r.m.s$ (i.e., $\sqrt{34.6^2 - 29.7^2} = 17\,ps\,r.m.s$) and $18\,ps\,r.m.s$ (i.e., $\sqrt{28.5^2 - 18.5^2} = 18\,ps\,r.m.s$).

Less data was obtained in comparison to the Paragraph IV-B. Data rate is, in reality, proportional to R_{CRT}, and each measure is 4 bytes long. This translates to a $4R_{CRT}\,Byte/s$ global data rate. The TDC generates the timestamps associated with the SNSPDs, the coincidence between timestamps is checked, and only the timestamps that pass the coincidence check (i.e., the difference between the timestamps coming from different SNSPDs below a maximum value T) are subtracted and put into the histogram using the proposed approach. The entire algorithm is conducted in real-time on the same FPGA that houses the TDC, with the PC serving solely as a read-out device. The pipeline for this elaboration process is shown in Figure 17.
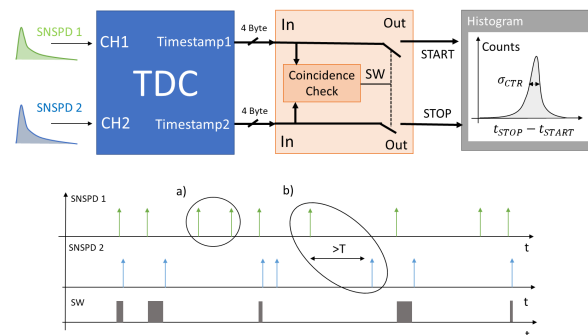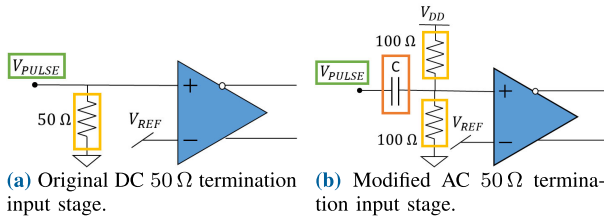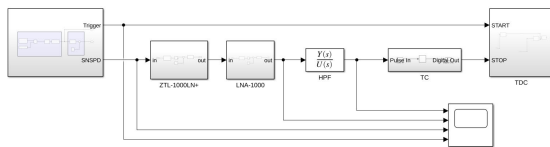

FIGURE 17. Elaboration process for the measure of the CTR. The coincidence checker set SW at '1' if a coincidence between timestamps is detected. In a) SW is at '0' because no SNSPD #2 event follows the SNSPD #1 ones; instead, in b) the distance between the timestamps is bigger than the maximum allowed (T).

TABLE 9. Measurements of σ_{CTR} at different $R_{SNSPD,1}$, $R_{SNSPD,2}$, and R_{CTR} performed in real-time by the TDC.

$R_{SNSPD,1}$ [kHz]	$R_{SNSPD,2}$ [kHz]	R_{CTR} [Hz]	σ_{CTR} [ps r.m.s.]
10	2.3	0.460	21.4
5.5	6.1	0.671	26.9
7.4	8.0	1.18	26.6
12	12	2.88	28.0
16	17	5.44	31.0
26	26	13.5	26.2
34	35	23.8	26.9
55	50	55.0	28.0
73	75	110	27.6
113	110	248	28.2
142	137	389	33.4
147	154	453	33.4
173	170	588	32.0
186	197	733	34.6

(a) Original DC $50\,\Omega$ termination input stage. (b) Modified AC $50\,\Omega$ termination input stage.

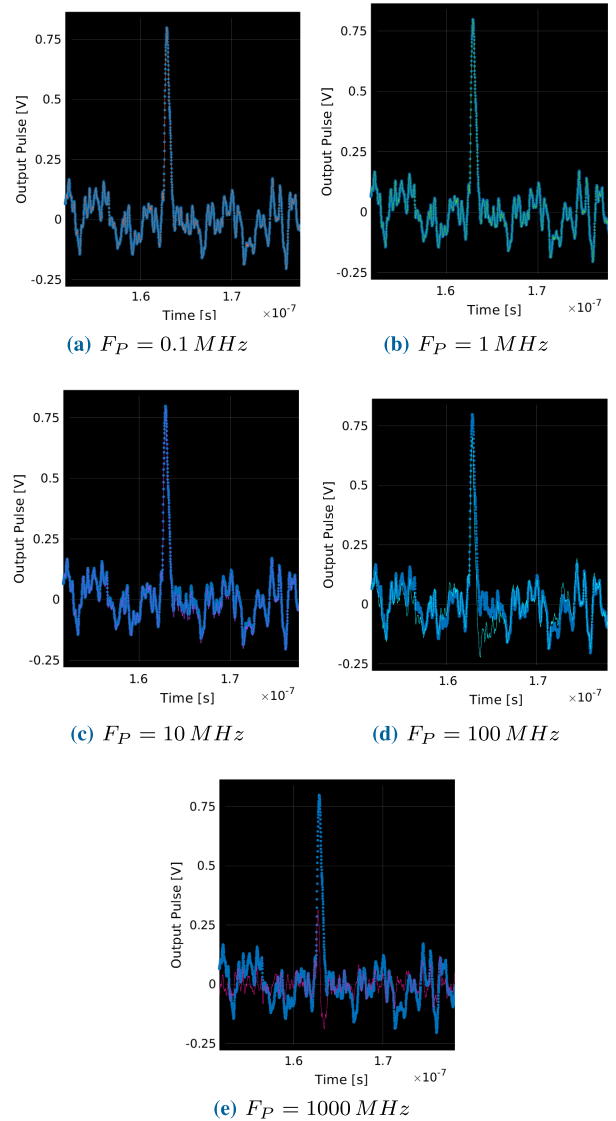**FIGURE 18.** Modified input front-end of the TDC.

FIGURE 19. Block diagram of the entire simulation environment with the photon detection emulation, the two amplifiers, the HPF, the TC, the TDC for timestamp measurement, and the scope to see "analog" waveforms.

TABLE 10. Simulated CTR for different values of C ($32\,nF$, $3.2\,nF$, $320\,pF$, $32\,pF$, $3.2\,pF$) normalized with respect to the DC value ($\sigma_{TOT}(F_P)/\sigma_{TOT}(0)$), i.e., $F_P = 1/(2\pi \cdot 50\Omega \cdot C)$, and considering different R_{SNSPD} values.

R_{SNSPD} [MHz]	$\sigma_{TOT}(F_P)/\sigma_{TOT}(0)$ [%]				
	$32\,nF$ $0.1\,MHz$	$3.2\,nF$ $1\,MHz$	$320\,pF$ $10\,MHz$	$32\,pF$ $0.1\,GHz$	$3.2\,pF$ $1\,GHz$
7.6	100	100	101	98.4	80.8
19.0	100	100	101	96.7	77.2
38.0	100	100	99.8	94.2	78.8
57.0	100	100	100	96.7	83.0
68.4	100	100	100	95.2	78.9
76.0	100	100	101	95.5	76.2

(a) $F_P = 0.1\,MHz$ (b) $F_P = 1\,MHz$

(c) $F_P = 10\,MHz$ (d) $F_P = 100\,MHz$

(e) $F_P = 1000\,MHz$

FIGURE 20. Simulated waveform at the output of the SNSPD (blue dots) and the relative HPF (continuous line) for different F_P values.

TABLE 11. The parameter σ_{TOT} measured at different R_{SNSPD} values using TDC with the HPF at $F_P = 100\,MHz$ ($\sigma_{TOT}(HPF)$), in DC ($\sigma_{TOT}(DC)$) and estimation of the corresponding σ_{WALK}.

R_{SNSPD} [kHz]	σ_{TOT} [ps r.m.s.]		σ_{WALK} [ps r.m.s.] $\sqrt{\sigma_{TOT}^2(DC) - \sigma_{TOT}^2(HPF)}$
	HPF	DC	
5	25.9	33.8	21.7
36	26.0	34.6	22.8
450	26.0	34.8	23.1
1000	22.4	33.4	24.8

VI. BASELINE FILTERING

In this section, we show how the precision was enhanced by filtering out the baseline fluctuation introduced in Paragraph VI-A for both LASER vs SNSPD and SNSPD vs SNSPD. In order to appropriately tune the proposed circuit, some simulations utilizing the SNSPD model found in Paragraph III-B were performed before designing the hardware.

A. BASELINE FILTERING CIRCUIT

To compensate for the baseline fluctuation, we assume that is low-frequency noise caused by the superposition effect created by exponential decay with a τ of a few tens of nanoseconds, i.e. $F_L = 10\,MHz$. In these terms, the easiest method is to employ a first-order High-Pass Filter (HPF) that

reshapes the τ to ensure a shorter exponential decay (that is 5τ long). As a result, we replaced the $50\,\Omega$ DC termination with an AC one in the TDC board's input area, as shown in Figure 18.

As you can see, the HPF attenuates each harmonic below the pole frequency $F_P = 1/2\pi RC$, by $20\,dB/dec$, where C is the capacitance that creates the AC coupling and R is the equivalent resistance ($100\Omega\|100\Omega$) that makes the $50\,\Omega$ termination. Different simulations are performed in Paragraph VI-B in order to tune the best value of C.

B. SIMULATION

To begin, the HPF, TC, and TDC models have been added to the SNSPD simulation model described in Paragraph III-B. The LASER's digital output is directly connected to the TDC's START, but the SNSPD exponential form of the output is filtered by the HPF to remove the baseline, as shown in Figure 19. The output of the HPF is then transformed into a digital trigger by the TC and connected to the TDC's STOP, just like in the experimental set-up. The TDC freezes the simulation's timestamp when a trigger event occurs on the START, generating T_{START}, and on the STOP, generating T_{STOP}. The final measure $\Delta T = T_{STOP} - T_{START}$ is then calculated, and the target is legitimate only if the STOP event occurs after the START in a laser period (i.e., $T_{START} \leq T_{STOP} < T_{START} + T_{LASER}$). To set the value of C, the standard deviation of ΔT ($\sigma_{\Delta T}$) is employed as a driving parameter.

Table 10 shows several values of $\sigma_{\Delta T}$ as functions of the simulated R_{SNSPD}, with various values of C and the DC value (no HPF) considered as reference. We can see how the HPF fails to filter out the baseline for $F_P \leq F_L = 10\,MHz$, rendering the HPF worthless. As a result, we may argue that increasing F_P improves precision by filtering out walk-error. However, increasing F_P reduces the loudness of the output signal, making discrimination more difficult. Figure 20 illustrates this point. As a result, $C = 32\,ps$ was chosen for the hardware tests.

VII. SNSPD TIMESTAMPING WITH TDC WITH BASELINE FILTERING

We performed the experiment described in Section IV, but modified the TDC's input front-end as shown in ParagraphVI-A, and used a value of $32\,pF$ for the C ($F_P = 100\,MHz$) as calculated in Paragraph VI-B.

A. SNSPD VS LASER

Table 11 highlights the measurement precision of LASER vs SNSPD with (HPF present at $F_P = 100\,MHz$) and without (DC) baseline filtering used as reference. We can theoretically estimate σ_{TOT} using Equation (10), given sigma $\sigma_{BASE} \rightarrow 0$, which is $24.2\,ps\,r.m.s.$ (i.e., $\sqrt{8^2 + 14^2 + 0 + 17^2 + 6^2} = 24.2\,ps\,r.m.s.$). The discrepancy between expected and measured values corresponds to quadratic error in the range of $0\,ps\,r.m.s.$
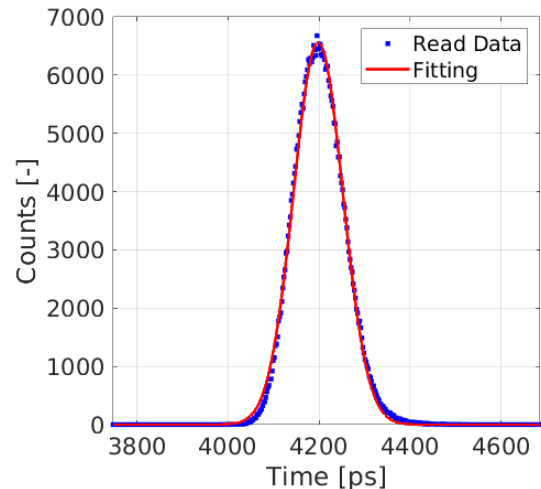
(a) HPF at $F_P = 10\,MHz$, precision of $34.6\,ps\,r.m.s.$
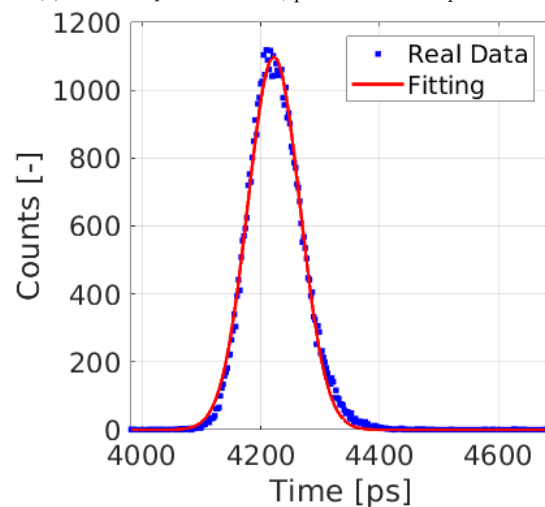
(b) HPF at $F_P = 100\,MHz$, precision of $26.0\,ps\,r.m.s$

FIGURE 21. Histogram of the LASER vs SNSPD measurements at the rate of 35 kHz.

(i.e, $\sqrt{22.4^2 - 24.2^2} = 0\,ps\,r.m.s.$) to $9.5\,ps\,r.m.s.$ (i.e, $\sqrt{26^2 - 24.2^2} = 9.5\,ps\,r.m.s.$).
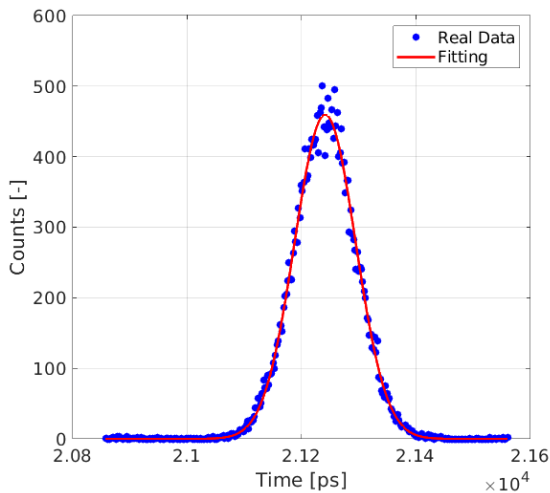
The last column of Table 11, that use the quadratic difference between HPF and DC coupled values of σ_{TOT}, shows the intensity of the rejected σ_{WALK} in the range from 21.7 to $24.8\,ps\,r.m.s.$. This must be compared to Table (5) (Paragraph (IV-A)), which shows that the range is $3.9\,ps\,r.m.s.$ to $8.9\,ps\,r.m.s.$ This discrepancy is due solely to the fact that σ_{WALK} is extracted by measuring σ_{BASE}, and the Sl is impacted by a larger uncertainty than the direct measurement. In addition, we can see that when R_{SNSPD} rises, the chance of the pile-up effect rises with it worsing σ_{TOT}. The histograms used to determine the σ_{TOT} at $R_{SNSPD} = 36\,kHz$ with a precision of $34.6\,ps\,r.m.s.$ using the HPL of $F_P = 10\,MHz$ and $26.0\,ps\,r.m.s.$ using the HPL of $F_P = 100\,MHz$ are shown in Figure 21.

B. SNSPD VS SNSPD

Measured the σ_{CTR} using different C values ($32\,nF$, $3.2\,nF$, $320\,pF$, $32\,pF$, $3.2\,pF$) at different rates ($R_{SNSPD,1}$, $R_{SNSPD,2}$,

TABLE 12. Measured σ_{CTR} for different values of C (32 nF, 3.2 nF, 320 pF, 32 pF, 3.2 pF), i.e. $F_P = 1/(2\pi \cdot 50\Omega \cdot C)$, considering different count rates ($R_{SNSPD,1} = R_{SNSPD,2} = R_{SNSPD}$) and R_{CRT}.

| R_{SNSPD} [Hz]	$C = 32\,nF$ $F_P = 100\,kHz$ R_{CTR} [Hz]	σ_{CTR} [ps r.m.s.]	$C = 3.2\,nF$ $F_P = 1\,MHz$ R_{CTR} [Hz]	σ_{CTR} [ps r.m.s.]	$C = 320\,pF$ $F_P = 10\,MHz$ R_{CTR} [Hz]	σ_{CTR} [ps r.m.s.]	$C = 32\,pF$ $F_P = 100\,MHz$ R_{CTR} [Hz]	σ_{CTR} [ps r.m.s.]	$C = 3.2\,pF$ $F_P = 1\,GHz$ R_{CTR} [Hz]	σ_{CTR} [ps r.m.s.]
10	2.9	22.8								
20			8	25.7			8	22.6	8	25.6
50	50	22.8	50	25.2	50	22.9				
73					110	24.0				
0.1 k	0.2 k	23.7	0.2 k	24.9			0.2 k			22.2
0.2 k							0.8 k			24.7
0.5 k	5 k	29.4	5 k	32.3			5 k	26.9	5 k	29.6
0.1 M					200	24.4				
0.15 M					450	24.4				
0.2 M					800	24.3				
0.3 M					1.8 k	25.9				
0.5 M					5.8 k	30.2				
1 M	20 k	27.7	20 k	31.5	20 k	29.5	20 k	23.6	20 k	29.5
2 M							88 k	29.7		26.3
4.5 M	0.4 M	44.7			0.4 M	38.8				
7 M							0.98 M	33.4		

FIGURE 22. The CTR measurement between SNSPDs at 450 kcps using the HPF at $C = 320\,pF$ ($F_P = 10\,MHz$) has a σ_{CRT} of $38.8\,ps\,r.m.s$, according to the plotted histogram.

R_{CTR}) are reported in Table 12. We can observe how the σ_{CTR} becomes more precise as the F_P increases, implying that the baseline fluctuation is minimized. Unfortunately, if F_P is set too high, the HPF suppresses not only the baseline but also the harmonics that make up the SNSPD's short rising time, resulting in a reduction in signal amplitude (A). In this way, we decrease not just σ_{BASE} but also Sl while raising σ_{WALK}. Furthermore, if A is too low, the exponential signal should be impossible to discern from the noise floor. We can observe that the possibility of the pile-up effect grows as the rates rise. In this way, a greater σ_{CTR} can be obtained at a lower rate for the same F_P. Figure 22 shows the histogram used to determine the CTR of $38.8\,ps\,r.m.s$ at $R_{CRT} = 450\,kHz$ with an HPL characteristic of a $F_P = 10\,MHz$.

VIII. COMPARISON AND FUTURE DEVELOPMENT

Figure 23 shows a comparison of CTRs as a function of R_{CRT}, taking into consideration the various ways discussed in Sections IVV and VII. The blue line with "o" markers represents the CTRs obtained with DO from Table 6. The CTR is unaffected by the rate thanks to the DO's baseline filtering; nevertheless, the DO's memory and processing capabilities limit the maximum acquisition rate of $700\,Hz$. The orange line with "+" markers represents the CTRs acquired with the TDC without any filters as reported in Table 9. We can observe a low resolution CTR because of the baseline fluctuation; the CTRs are computed directly in the FPGA.

The CTRs acquired with the TDC with HPFs at $F_P = 100\,kHz$, $F_P = 1\,MHz$, $F_P = 10\,MHz$, $F_P = 100\,MHz$, and $F_P = 1\,GHz$ are shown by the other four lines, yellow with "x" as markers, purple with "□" as markers, green with "◇" as markers, light blue with "☆" as markers, and magenta with "✳" as markers. Table 9 has all of the values computed in real-time directly in the FPGA. We can observe how the baseline fluctuations are filtered for R_{CRT} less than F_P by looking at these lines. In reality, the lower F_P of the yellow ($F_P = 100\,kHz$), purple ($F_P = 1\,MHz$), and green ($F_P = 10\,MHz$) lines does not guarantee a proper reduction of baseline fluctuations. The light blue $F_P = 100\,MHz$), and the magenta ($F_P = 1\,GHz$) lines are the exceptions. The baseline filtering is effective at rates up to $100\,kHz$ for the light blue line ($F_P = 100\,MHz$). Instead, the magenta line ($F_P = 1\,GHz$) has a lower precision than the light blue lines ($F_P = 100\,MHz$), which is used to reduce the loudness of the filtered signal (see Figure 20). Figure 12 shows a comparison of time-walk estimates using the DO (blue line with "o" as markers) and TDC (orange line with "+" as markers) from Tables 5 and 11. The rate increases the time-walk in both cases, which is proportional to the baseline fluctuation. Various techniques and, without a doubt, inherent measurement
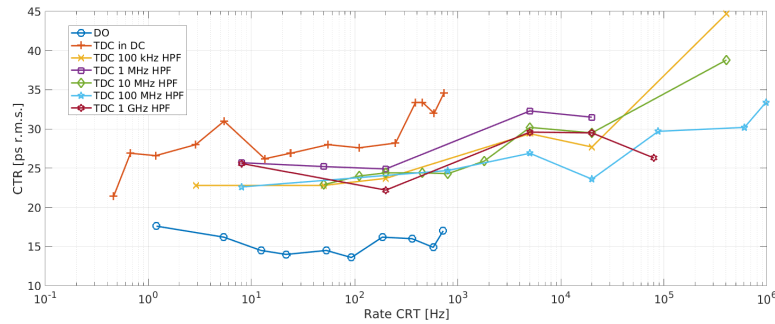
FIGURE 23. Comparison of CTRs as a function of R_{CRT}, taking into account the different approaches presented in Sections IVVVII.
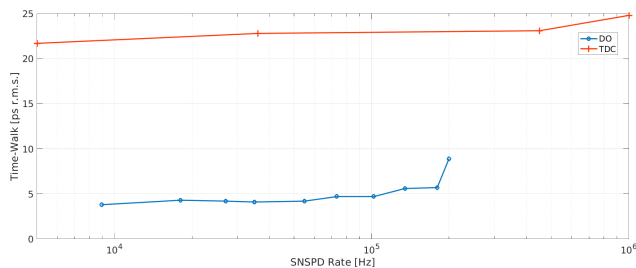
FIGURE 24. Comparison of time-walk estimation as a function of R_{SNSPD} using the methods described in Sections IVV.

faults are to blame for the numerical disparity between the DO and TDC results. In fact, we must keep in mind that the DO (blue line) time-walk estimation is achieved using a VM technique that extracts the baseline using the DSP algorithm and converts it to time-walk using equations (4). Instead, for the TDC (orange line), the time-walk is determined as the difference between the precision achieved with the HPF at $F_P = 100\,MHz\,(\sigma_{TOT}(HPF))$ and without it $(\sigma_{TOT}(DC))$, i.e., $\sqrt{\sigma_{TOT}^2(DC) - \sigma_{TOT}^2(HPF)}$. The CTR measurement is done between two SNSPDs to keep the budget under control, but the hardware supports 16 independent channels; the performance is confirmed using an emulation unsigned function generator (rather than 16 SNSPDs). In the future, the experimental evaluation of 16 SNSPDs will be investigated, with the measurement set-up and firmware modified to manage 16 detectors in parallel. Issues of cross-talk will be given specific attention.

IX. CONCLUSION

We explain how, at the cutting edge of technology, a time mode approach architecture integrally based on FPGA can conduct timing measurement and CTR on SNSPD (the most time-resolved detector). Both the TDC and measuring techniques such as coincidence and histogramming are performed inside the FPGA due to the versatility of the programmable logic manner. In this situation, the PC is only used as a monitor. Precision of less than 26 ps r.m.s. is attained using this technology in single-shot mode up to 1 MHz measuring rate. Furthermore, thanks to firmware flexibility, we can directly measure the CTR in FPGA; this allows us to identify whether two photons detected by two distinct SNSPDs are in coincidence or not with a precision of always.To ensure

this high precision by removing the intrinsic baseline fluctuation and decreasing the time-walk, a low-cost filtering on the SNSPD's output pulse is required. All processing takes place in parallel and effectively inside the FPGA, making this technology ideal for modern multi-channel applications; and the number of input channels may be easily extended from a firmware standpoint. Furthermore, we have specified that if cross-talk effects are present, particular attention would be paid.

REFERENCES

[1] C. M. Natarajan, M. G. Tanner, and R. H. Hadfield, "Superconducting nanowire single-photon detectors: Physics and applications," *Supercond. Sci. Technol.*, vol. 25, no. 6, Apr. 2012, Art. no. 063001, doi: 10.1088/0953-2048/25/6/063001.

[2] R. Hadfield and G. Johansson, *Superconducting Devices in Quantum Optics*, 1st ed. Berlin, Germany: Springer, Feb. 2016. [Online]. Available: https://citations.springernature.com/book?doi=10.1007/978-3-319-24091-6

[3] H. Takesue, S. W. Nam, Q. Zhang, R. H. Hadfield, T. Honjo, K. Tamaki, and Y. Yamamoto, "Quantum key distribution over a 40-dB channel loss using superconducting single-photon detectors," *Nature Photon.*, vol. 1, no. 6, pp. 343–348, Jun. 2007. [Online]. Available: https://www.nature.com/articles/nphoton.2007.75

[4] H.-S. Zhong et al., "Quantum computational advantage using photons," *Science*, vol. 370, no. 6523, pp. 1460–1463, Dec. 2020. [Online]. Available: https://www.science.org/doi/full/10.1126/science.abe8770?casa_token=DI6HHdDovi4AAAAA%3AMLpCXbwHKdYDpqzuf7-jmuZZ9H4XdKVatUdp9Weob34i2QllMrg7TX8gbnVfD6C1eGBvFu6MYAZbdQ, doi: 10.1126/science.abe8770.

[5] G. Reithmaier, M. Kaniber, F. Flassig, S. Lichtmannecker, K. Müller, A. Andrejew, J. Vučković, R. Gross, and J. J. Finley, "On-chip generation, routing, and detection of resonance fluorescence," *Nano Lett.*, vol. 15, no. 8, pp. 5208–5213, Aug. 2015, doi: 10.1021/acs.nanolett.5b01444.

[6] J. W. Silverstone, D. Bonneau, K. Ohira, N. Suzuki, H. Yoshida, N. Iizuka, M. Ezaki, C. M. Natarajan, M. G. Tanner, R. H. Hadfield, V. Zwiller, G. D. Marshall, J. G. Rarity, J. L. O'Brien, and M. G. Thompson, "On-chip quantum interference between silicon photon-pair sources," *Nature Photon.*, vol. 8, no. 2, pp. 104–108, Feb. 2014. [Online]. Available: https://www.nature.com/articles/nphoton.2013.339

[7] J. M. Shainline, S. M. Buckley, A. N. McCaughan, J. T. Chiles, A. J. Salim, M. Castellanos-Beltran, C. A. Donnelly, M. L. Schneider, R. P. Mirin, and S. W. Nam, "Superconducting optoelectronic loop neurons," *J. Appl. Phys.*, vol. 126, no. 4, Jul. 2019, Art. no. 044902, doi: 10.1063/1.5096403.

[8] M. Rosticher, F. R. Ladan, J. P. Maneval, S. N. Dorenbos, T. Zijlstra, T. M. Klapwijk, V. Zwiller, A. Lupaşcu, and G. Nogues, "A high efficiency superconducting nanowire single electron detector," *Appl. Phys. Lett.*, vol. 97, no. 18, Nov. 2010, Art. no. 183106, doi: 10.1063/1.3506692.

[9] L. Shen, J. Lee, A. W. Hartanto, P. Tan, C. Kurtsiefer, and C. Kurtsiefer, "Wide-range wavelength-tunable photon-pair source for characterizing single-photon detectors," *Opt. Exp.*, vol. 29, no. 3, pp. 3415–3424, Feb. 2021. [Online]. Available: https://opg.optica.org/oe/abstract.cfm?uri=oe-29-3-3415

[10] F. Marsili, F. Bellei, F. Najafi, A. Dane, E. Dauler, R. J. Molnar, and K. K. Berggren, "Efficient single photon detection from 0.5 To 5 micron wavelength," in *Conf. Lasers Electro-Opt., OSA Tech. Dig.* Optica Publishing Group, 2012, Paper QTu1E.2. [Online]. Available: https://opg.optica.org/abstract.cfm?uri=QELS-2012-QTu1E.2

[11] L. Duclaux, "Review of the doping of carbon nanotubes (multiwalled and single-walled)," *Carbon*, vol. 40, no. 10, pp. 1751–1764, Aug. 2002. [Online]. Available: https://www.sciencedirect.com/science/article/pii/S000862230200043X

[12] S. Castelletto and A. Boretti, "Silicon carbide color centers for quantum applications," *J. Physics: Photon.*, vol. 2, no. 2, Mar. 2020, Art. no. 022001, doi: 10.1088/2515-7647/ab77a2.

[13] F. P. García de Arquer, D. V. Talapin, V. I. Klimov, Y. Arakawa, M. Bayer, and E. H. Sargent, "Semiconductor quantum dots: Technological progress and future challenges," *Science*, vol. 373, no. 6555, Aug. 2021, Art. no. eaaz8541, doi: 10.1126/science.aaz8541.

[14] I. E. Zadeh, J. Chang, J. W. N. Los, S. Gyger, A. W. Elshaari, S. Steinhauer, S. N. Dorenbos, and V. Zwiller, "Superconducting nanowire single-photon detectors: A perspective on evolution, state-of-the-art, future developments, and applications," *Appl. Phys. Lett.*, vol. 118, no. 19, May 2021, Art. no. 190502, doi: 10.1063/5.0045990.

[15] A. McCarthy, N. J. Krichel, N. R. Gemmell, X. Ren, M. G. Tanner, S. N. Dorenbos, V. Zwiller, R. H. Hadfield, and G. S. Buller, "Kilometer-range, high resolution depth imaging via 1560 nm wavelength single-photon detection," *Opt. Exp.*, vol. 21, no. 7, pp. 8904–8915, Apr. 2013. [Online]. Available: https://opg.optica.org/oe/abstract.cfm?uri=oe-21-7-8904

[16] G. G. Taylor, D. Morozov, N. R. Gemmell, K. Erotokritou, S. Miki, S. Miki, H. Terai, and R. H. Hadfield, "Photon counting LIDAR at 2.3 μm wavelength with superconducting nanowires," *Opt. Exp.*, vol. 27, no. 26, pp. 38147–38158, Dec. 2019. [Online]. Available: https://opg.optica.org/oe/abstract.cfm?uri=oe-27-26-38147

[17] F. Villa, F. Severini, F. Madonini, and F. Zappa, "SPADs and SiPMs arrays for long-range high-speed light detection and ranging (LiDAR)," *Sensors*, vol. 21, no. 11, p. 3839, Jun. 2021. [Online]. Available: https://www.mdpi.com/1424-8220/21/11/3839

[18] A. Incoronato, M. Locatelli, and F. Zappa, "Statistical modelling of SPADs for time-of-flight LiDAR," *Sensors*, vol. 21, no. 13, p. 4481, Jun. 2021. [Online]. Available: https://www.mdpi.com/1424-8220/21/13/4481

[19] N. R. Gemmell, A. McCarthy, B. Liu, M. G. Tanner, S. D. Dorenbos, V. Zwiller, M. S. Patterson, G. S. Buller, B. C. Wilson, and R. H. Hadfield, "Singlet oxygen luminescence detection with a fiber-coupled superconducting nanowire single-photon detector," *Opt. Exp.*, vol. 21, no. 4, pp. 5005–5013, Feb. 2013. [Online]. Available: https://opg.optica.org/oe/abstract.cfm?uri=oe-21-4-5005

[20] J. Hu, Q. Zhao, X. Zhang, L. Zhang, X. Zhao, L. Kang, and P. Wu, "Photon-counting optical time-domain reflectometry using a superconducting nanowire single-photon detector," *J. Lightw. Technol.*, vol. 30, no. 16, pp. 2583–2588, Aug. 1, 2012.

[21] L. J. Deutsch, "Towards deep space optical communications," *Nature Astron.*, vol. 4, no. 9, p. 907, Sep. 2020. [Online]. Available: https://www.nature.com/articles/s41550-020-1193-1

[22] D. M. Boroson, R. S. Bondurant, and J. J. Scozzafava, "Overview of high-rate deep-space laser communications options," *Proc. SPIE*, vol. 5338, p. 37, Jun. 2004. [Online]. Available: doi: 10.1117/12.543010.

[23] I. E. Zadeh et al., "Efficient single-photon detection with 7.7 ps time resolution for photon-correlation measurements," *ACS Photon.*, vol. 7, no. 7, pp. 1780–1787, Jul. 2020. [Online]. Available: https://pubs.acs.org/doi/10.1021/acsphotonics.0c00433, doi: 10.1021/acsphotonics.0c00433.

[24] R. H. Hadfield, M. J. Stevens, S. S. Gruber, A. J. Miller, R. E. Schwall, R. P. Mirin, and S. W. Nam, "Single photon source characterization with a superconducting single photon detector," *Opt. Exp.*, vol. 13, no. 26, pp. 10846–10853, Dec. 2005. [Online]. Available: https://opg.optica.org/oe/abstract.cfm?uri=oe-13-26-10846

[25] D. Breton, V. De Cacqueray, E. Delagnes, H. Grabas, J. Maalmi, N. Minafra, C. Royon, and M. Saimpert, "Measurements of timing resolution of ultra-fast silicon detectors with the SAMPIC waveform digitizer," *Nucl. Instrum. Methods Phys. Res. A, Accel. Spectrom. Detect. Assoc. Equip.*, vol. 835, pp. 51–60, Nov. 2016. [Online]. Available: https://www.sciencedirect.com/science/article/pii/S0168900216308373

[26] H. Li, X. Yang, L. You, H. Wang, P. Hu, W. Zhang, Z. Wang, and X. Xie, "Improving detection efficiency of superconducting nanowire single-photon detector using multilayer antireflection coating," *AIP Adv.*, vol. 8, no. 11, Nov. 2018, Art. no. 115022, doi: 10.1063/1.5034374.

[27] Y. Fei. (2020). *CMOS Time-Mode Circuits and Systems: Fundamentals and Applications*. [Online]. Available: https://www.routledge.com/CMOS-Time-Mode-Circuits-and-Systems-Fundamentals-and-Applications/Yuan/p/book/9780367737603

[28] D. Breton, E. Delagnes, J. Maalmi, K. Nishimura, L. L. Ruckman, G. Varner, and J. Va'vra, "High resolution photon timing with MCP-PMTs: A comparison of a commercial constant fraction discriminator (CFD) with the ASIC-based waveform digitizers TARGET and WaveCatcher," *Nucl. Instrum. Methods Phys. Res. A, Accel. Spectrom. Detect. Assoc. Equip.*, vol. 629, no. 1, pp. 123–132, Feb. 2011. [Online]. Available: https://www.sciencedirect.com/science/article/pii/S0168900210023521

[29] Z. J. Chen, X. Y. Peng, X. Zhang, T. F. Du, Z. M. Hu, Z. Q. Cui, L. J. Ge, X. F. Xie, X. Yuan, G. Gorini, M. Nocente, M. Tardocchi, L. Q. Hu, G. Q. Zhong, S. Y. Lin, B. N. Wan, X. Q. Li, G. H. Zhang, J. X. Chen, and T. S. Fan, "Data acquisition system with pulse height capability for the TOFED time-of-flight neutron spectrometer," *Rev. Sci. Instrum.*, vol. 85, no. 11, Nov. 2014, Art. no. 11D830.

[30] G. Pasquali, R. Ciaranfi, L. Bardelli, M. Bini, A. Boiano, F. Giannelli, A. Ordine, and G. Poggi, "A DSP equipped digitizer for online analysis of nuclear detector signals," *Nucl. Instrum. Methods Phys. Res. A, Accel. Spectrom. Detect. Assoc. Equip.*, vol. 570, no. 1, pp. 126–132, Jan. 2007. [Online]. Available: https://www.sciencedirect.com/science/article/pii/S0168900206017669

[31] F. Garzetti, N. Corna, N. Lusardi, and A. Geraci, "Time-to-digital converter IP-core for FPGA at state of the art," *IEEE Access*, vol. 9, pp. 85515–85528, 2021.

[32] N. Corna, F. Garzetti, N. Lusardi, and A. Geraci, "Digital instrument for time measurements: Small, portable, High–performance, fully programmable," *IEEE Access*, vol. 9, pp. 123964–123976, 2021.

[33] N. Lusardi, F. Garzetti, and A. Geraci, "Digital instrument with configurable hardware and firmware for multi-channel time measures," *Rev. Sci. Instrum.*, vol. 90, no. 5, May 2019, Art. no. 055113, doi: 10.1063/1.5028131.

[34] A. J. Kerman, D. Rosenberg, R. J. Molnar, and E. A. Dauler, "Readout of superconducting nanowire single-photon detectors at high count rates," *J. Appl. Phys.*, vol. 113, no. 14, Apr. 2013, Art. no. 144511, doi: 10.1063/1.4799397.

[35] M. Sidorova, A. Semenov, H.-W. Hübers, I. Charaev, A. Kuzmin, S. Doerner, and M. Siegel, "Physical mechanisms of timing jitter in photon detection by current-carrying superconducting nanowires," *Phys. Rev. B, Condens. Matter*, vol. 96, no. 18, Nov. 2017, Art. no. 184504, doi: 10.1103/PhysRevB.96.184504.

[36] M. Caloz, M. Perrenoud, C. Autebert, B. Korzh, M. Weiss, C. Schönenberger, R. J. Warburton, H. Zbinden, and F. Bussières, "High-detection efficiency and low-timing jitter with amorphous superconducting nanowire single-photon detectors," *Appl. Phys. Lett.*, vol. 112, no. 6, Feb. 2018, Art. no. 061103, doi: 10.1063/1.5010102.

[37] D. F. Santavicca, B. Noble, C. Kilgore, G. A. Wurtz, M. Colangelo, D. Zhu, and K. K. Berggren, "Jitter characterization of a dual-readout SNSPD," *IEEE Trans. Appl. Supercond.*, vol. 29, no. 5, pp. 1–4, Aug. 2019.

[38] H. Zhang, J. Liu, J. Guo, L. Xiao, J. Xie, and J. Xie, "Photon energy-dependent timing jitter and spectrum resolution research based on time-resolved SNSPDs," *Opt. Exp.*, vol. 28, no. 11, pp. 16696–16707, May 2020. [Online]. Available: https://opg.optica.org/oe/abstract.cfm?uri=oe-28-11-16696

[39] N. Calandri, Q.-Y. Zhao, D. Zhu, A. Dane, and K. K. Berggren, "Superconducting nanowire detector jitter limited by detector geometry," *Appl. Phys. Lett.*, vol. 109, no. 15, Oct. 2016, Art. no. 152601, doi: 10.1063/1.4963158.

[40] L. You, "Superconducting nanowire single-photon detectors for quantum information," *Nanophotonics*, vol. 9, no. 9, pp. 2673–2692, Jul. 2020. [Online]. Available: https://www.degruyter.com/document/doi/10.1515/nanoph-2020-0186/html?lang=en, doi: 10.1515/nanoph-2020-0186.

[41] T. J. Paulus, "Timing electronics and fast timing methods with scintillation detectors," *IEEE Trans. Nucl. Sci.*, vol. NS-32, no. 3, pp. 1242–1249, Jun. 1985.

[42] E. A. Dauler, M. E. Grein, A. J. Kerman, F. Marsili, S. Miki, S. W. Nam, M. D. Shaw, H. Terai, V. B. Verma, and T. Yamashita, "Review of superconducting nanowire single-photon detector system design options and demonstrated performance," *Opt. Eng.*, vol. 53, no. 8, Jun. 2014, Art. no. 081907. [Online]. Available: https://www.spiedigitallibrary.org/journals/optical-engineering/volume-53/issue-08/081907/Review-of-superconducting-nanowire-single-photon-detector-system-design-options/10.1117/1.OE.53.8.081907.full, doi: 10.1117/1.OE.53.8.081907.

[43] G. Pilyavsky, A. Sinclair, E. Weeks, C. Wheeler, E. Lunde, and P. Mauskopf, "Time tagging individual photons with a low-cost FPGA based time to digital converter," *Proc. SPIE*, vol. 10701, pp. 785–794, Jul. 2018. [Online]. Available: http://www.scopus.com/inward/record.url?scp=85052903034&partnerID=8YFLogxK

[44] N. A. W. Dutton, S. Gnecchi, L. Parmesan, A. J. Holmes, B. Rae, L. A. Grant, and R. K. Henderson, "11.5 A time-correlated single-photon-counting sensor with 14 GS/S histogramming time-to-digital converter," in *IEEE Int. Solid-State Circuits Conf. (ISSCC) Dig. Tech. Papers*, Feb. 2015, pp. 1–3.

[45] A. Salvi, K. Chavan, and P. Vaidya, "Design and construction of programmable time-to-amplitude converter," in *Proc. 4th Int. Conf. Trends Electron. Informat. (ICOEI)*, Jun. 2020, pp. 53–57.

[46] N. Lusardi, F. Garzetti, and A. Geraci, "The role of sub-interpolation for delay-line time-to-digital converters in FPGA devices," *Nucl. Instrum. Methods Phys. Res. A, Accel. Spectrom. Detect. Assoc. Equip.*, vol. 916, pp. 204–214, Feb. 2019. [Online]. Available: https://www.sciencedirect.com/science/article/pii/S0168900218317479

[47] A. Aloisio, P. Branchini, R. Giordano, V. Izzo, and S. Loffredo, "High-precision time-to-digital converter in a FPGA device," in *Proc. 16th IEEE-NPSS Real Time Conf.*, May 2009, pp. 283–286.

[48] F. Garzetti, N. Lusardi, N. Corna, S. Salgaro, N. Busola, A. Geraci, G. Brajnik, S. Carrato, G. Cautero, M. Cautero, R. Sergo, and L. Stebel, "Fully FPGA-based 3D (X,Y,t) imaging system with cross delay-lines detectors and eight-channels high-performance time-to-digital converter," in *Proc. IEEE Nucl. Sci. Symp. Med. Imag. Conf. (NSS/MIC)*, Oct. 2020, pp. 1–4.

[49] J. Wu, L. You, S. Chen, H. Li, Y. He, C. Lv, Z. Wang, and X. Xie, "Improving the timing jitter of a superconducting nanowire single-photon detection system," *Applied Opt.*, vol. 56, no. 8, pp. 2195–2200, Mar. 2017. [Online]. Available: https://opg.optica.org/ao/abstract.cfm?uri=ao-56-8-2195

[50] A. Verevkin, A. Pearlman, W. Slysz, J. Zhang, M. Currie, A. Korneev, G. Chulkova, O. Okunev, P. Kouminov, K. Smirnov, B. Voronov, G. N. Gol'tsman, and R. Sobolewski, "Ultrafast superconducting single-photon detectors for near-infrared-wavelength quantum communications," *J. Modern Opt.*, vol. 51, nos. 9–10, pp. 1447–1458, Jun. 2004, doi: 10.1080/09500340408235284.

[51] W. Slysz et al., "Fiber-coupled NbN superconducting single-photon detectors for quantum correlation measurements," *Proc. SPIE*, vol. 6583, May 2007, Art. no. 65830J. [Online]. Available: https://www.spiedigitallibrary.org/conference-proceedings-of-spie/6583/1/Fiber-coupled-NbN-superconducting-single-photon-detectors-for-quantum-correlation/10.1117/12.723729.short?SSO=1, doi: 10.1117/12.723729.

[52] W. H. P. Pernice, C. Schuck, O. Minaeva, M. Li, G. N. Goltsman, A. V. Sergienko, and H. X. Tang, "High-speed and high-efficiency travelling wave single-photon detectors embedded in nanophotonic circuits," *Nature Commun.*, vol. 3, no. 1, p. 1325, Dec. 2012. [Online]. Available: https://www.nature.com/articles/ncomms2307

[53] L. You, X. Yang, Y. He, W. Zhang, D. Liu, W. Zhang, L. Zhang, L. Zhang, X. Liu, S. Chen, Z. Wang, and X. Xie, "Jitter analysis of a superconducting nanowire single photon detector," *AIP Adv.*, vol. 3, no. 7, Jul. 2013, Art. no. 072135.

[54] V. Shcheslavskiy, P. Morozov, A. Divochiy, Y. Vakhtomin, K. Smirnov, and W. Becker, "Ultrafast time measurements by time-correlated single photon counting coupled with superconducting single photon detector," *Rev. Sci. Instrum.*, vol. 87, no. 5, May 2016, Art. no. 053117, doi: 10.1063/1.4948920.

[55] I. E. Zadeh, J. W. N. Los, R. B. M. Gourgues, V. Steinmetz, G. Bulgarini, S. M. Dobrovolskiy, V. Zwiller, and S. N. Dorenbos, "Single-photon detectors combining high efficiency, high detection rates, and ultra-high timing resolution," *APL Photon.*, vol. 2, no. 11, Nov. 2017, Art. no. 111301.

[56] N. Lusardi, J. W. N. Los, R. B. M. Gourgues, G. Bulgarini, and A. Geraci, "Photon counting with photon number resolution through superconducting nanowires coupled to a multi-channel TDC in FPGA," *Rev. Scientific Instrum.*, vol. 88, no. 3, Mar. 2017, Art. no. 035003, doi: 10.1063/1.4977594.

[57] E. E. Wollman, E. E. Wollman, V. B. Verma, V. B. Verma, A. E. Lita, W. H. Farr, M. D. Shaw, R. P. Mirin, and S. W. Nam, "Kilopixel array of superconducting nanowire single-photon detectors," *Opt. Exp.*, vol. 27, no. 24, pp. 35279–35289, Nov. 2019. [Online]. Available: https://opg.optica.org/oe/abstract.cfm?uri=oe-27-24-35279

[58] (2022). SQ. *Single Quantum Eos*. [Online]. Available: https://singlequantum.com/products/single-quantum-eos/

[59] (2022). LeCroy. *Teledyne LeCroy WaveRunner 9000 Oscilloscopes*. [Online]. Available: https://teledynelecroy.com/wr9000

[60] (2022). M. Circuit. *Mini Circuits—Global Leader of RF and Microwave Components*. [Online]. Available: https://www.minicircuits.com/

[61] (2022). BAY. *RF Frequency Divider & Custom Microwave Amplifier | RF BAY INC*. [Online]. Available: https://www.rfbayinc.com/

[62] L. Redaelli, G. Bulgarini, S. Dobrovolskiy, S. N. Dorenbos, V. Zwiller, E. Monroy, and J. M. Gérard, "Design of broadband high-efficiency superconducting-nanowire single photon detectors," *Superconductor Sci. Technol.*, vol. 29, no. 6, May 2016, Art. no. 065016, doi: 10.1088/0953-2048/29/6/065016.

[63] N. Lusardi, N. Corna, F. Garzetti, S. Salgaro, and A. Geraci, "Cross-talk issues in time measurements," *IEEE Access*, vol. 9, pp. 129303–129318, 2021.

[64] E. Venialgo, N. Lusardi, F. Garzetti, A. Geraci, S. E. Brunner, D. R. Schaart, and E. Charbon, "Toward a full-flexible and fast-prototyping TOF-PET block detector based on TDC-on-FPGA," *IEEE Trans. Radiat. Plasma Med. Sci.*, vol. 3, no. 5, pp. 538–548, Sep. 2019.

[65] (2022). Xilinx. *Xilinx—Adaptable. Intelligent*. [Online]. Available: https://www.xilinx.com/

[66] (2022). Trenz. *Trenz Electronic GmbH*. [Online]. Available: https://www.trenz-electronic.de/de/

FABIO GARZETTI (Member, IEEE) received the Ph.D. degree (cum laude), Politecnico di Milano, in 2022. He developed the thesis work at the Digital Electronics Laboratory, Department of Electronics, Information And Bioengineering (DEIB) on a topic regarding innovative solutions for calibration and triggering of asynchronous signals for time-to-digital converters (TDCs) in field programmable gate arrays (FPGA). He is currently a Temporary Researcher with the Digital Electronics Laboratory, DEIB.

NICOLA LUSARDI (Member, IEEE) received the Ph.D. degree, in 2018. He developed the thesis work at the Digital Electronics Laboratory, DEIB on a topic regarding high-resolution time-to-digital converters (TDCs) in field programmable gate arrays (FPGA). He is currently a Temporary Researcher with the Digital Electronics Laboratory, DEIB, a Professor of electronics with Politecnico di Milano, and an Associate Member of the Italian National Nuclear Physics Institute (INFN).

ENRICO RONCONI (Member, IEEE) received the master's degree in electronic engineering from Politecnico di Milano, in 2020. His research interests include advanced programmable logic (PL) and software architectures for data processing and transfer in field programmable gate arrays (FPGA) implemented scientific equipment, and time-to-digital and digital-to-time converters (TDC and DTC).

ANDREA COSTA (Member, IEEE) was born in Piacenza, in 1995. He received the B.Sc. degree in biomedical engineering and the M.Sc. degree in electronics engineering from Politecnico di Milano, in 2017 and 2020, respectively. His research interests include innovative hardware architectures for data processing in the field of FPGA time-domain devices and FPGA DAQ for high data rate environments.

CHRISTOPHE GALLAND received the Ph.D. degree from ETH Zürich for a thesis in solid-state quantum optics with individual carbon nanotubes, in 2010. Since May 2017, he has been leading the Laboratory of Quantum and Nano-Optics at EPFL. He investigates light–matter interaction at the nanoscale and in the quantum regime, with a focus on molecules embedded in plasmonic cavities and on nitrogen-vacancy centers in diamonds.

SANTIAGO TARRAGO VELEZ received the Ph.D. degree from the Laboratory of Quantum and Nano-Optics, EPFL, Lausanne, in 2020. Since November 2021, he has been a Postdoctoral Researcher with the Danmarks Tekniske Universitet.

ANGELO GERACI (Senior Member, IEEE) received the Ph.D. degree (cum laude) in electronics from Politecnico di Milano, in 1996. Since 2004, he has been an Associate Professor with the Department of Electronics, Information and Bio-engineering (DEIB), Politecnico di Milano. His research interests include digital electronics based on microcontrollers, DSP and FPGA devices, specifically in the areas of radiation detection and medical imaging.

• • •